

Review

# Non-Noble Metal and Nonmetallic Plasmonic Nanomaterials with Located Surface Plasmon Resonance Effects: Photocatalytic Performance and Applications

Rou Li <sup>1,†</sup>, Xianfeng Wang <sup>1,†</sup> and Ming Chen <sup>1,2,\*</sup>

<sup>1</sup> Key Laboratory of Environmental Biology and Pollution Control, College of Environmental Science and Engineering, Hunan University, Ministry of Education, Changsha 410082, China

<sup>2</sup> Key Laboratory of Reservoir Aquatic Environment, Chongqing Institute of Green and Intelligent Technology, Chinese Academy of Sciences, Chongqing 400714, China

\* Correspondence: mchensn@hnu.edu.cn or chenming@cigit.ac.cn

† These authors contributed equally to this work.

**Abstract:** Photocatalysts with located surface plasmon resonance effects (LSPRs) have been studied in recent years due to their superior light harvesting capacity and photocatalytic performance in solving environmental problems and energy shortages. Plasmonic-noble-based photocatalysts are limited in terms of their practical application on account of their high cost, fixed plasma frequency, and low abundance. In order to solve these shortcomings, non-noble metal and nonmetallic plasmonic photocatalysts with LSPRs and advantages such as a lower cost and wider light adsorption range from the UV to NIR region have been developed. This paper reviews the recent development of non-noble metal and nonmetallic plasmonic photocatalysts and advances the research direction of plasmonic photocatalysts to achieve high photocatalytic activity and stability, providing guidance for photocatalysis to solve environmental problems and energy shortages.

**Keywords:** photocatalysis; LSPRs; non-noble metal; nonmetallic materials



**Citation:** Li, R.; Wang, X.; Chen, M. Non-Noble Metal and Nonmetallic Plasmonic Nanomaterials with Located Surface Plasmon Resonance Effects: Photocatalytic Performance and Applications. *Catalysts* **2023**, *13*, 940. <https://doi.org/10.3390/catal13060940>

Academic Editors: Jose L. Hueso, Ewa Kowalska and Zhishun Wei

Received: 16 April 2023

Revised: 18 May 2023

Accepted: 22 May 2023

Published: 26 May 2023



**Copyright:** © 2023 by the authors. Licensee MDPI, Basel, Switzerland. This article is an open access article distributed under the terms and conditions of the Creative Commons Attribution (CC BY) license (<https://creativecommons.org/licenses/by/4.0/>).

## 1. Introduction

With the rapid development of the economy and technology, environmental problems and energy shortages have attracted wide attention of the public. As an environmentally friendly and effective strategy to solve these problems above, photocatalysis has become a hot topic for many researchers. As a common photocatalyst, the traditional semiconductor TiO<sub>2</sub> has been widely studied in the photocatalytic removal of pollutants since the 1970s [1]. Although the TiO<sub>2</sub> photocatalyst has the advantages of good photoactivity, non-toxicity, high chemical stability, and a relatively low cost, its development in the field of photocatalysis is still limited due to the disadvantages of large band gap energy, fast photogenerated electron–hole recombination, and the absorption of only 4~5% of the full spectrum of ultraviolet (UV) light (<400 nm) [1–4]. Therefore, it is increasingly important to seek a novel photocatalyst with broad light absorption, a high carrier separation efficiency, and a low photogenerated electron–hole recombination rate.

By virtue of surface plasmon resonance effects (SPRs), plasmonic materials have entered the field of photocatalysis due to their optical absorption range from the UV to the near-infrared (NIR) region and high charge separation efficiency [5]. SPR is the collective oscillation of free electrons on the surface of materials with the resonance of the electromagnetic field [6]. The collective motion of the electron cloud on the metal surface causes SPR when electromagnetic waves reach the surface from the outside. As the size of nanoparticles (NPs) decreases, the space available for free electron oscillation becomes smaller, and the energy of external electromagnetic waves that can induce collective resonance decreases. At this time, the collective resonance occurs at a specific excitation frequency and

is confined to NPs, and localized surface plasmon resonance effects (LSPRs) occur [7], as shown in Figure 1. LSPRs can modulate the light response range of photocatalytic systems by controlling the composition, morphology, and dielectric environment of NPs [5,8], and plasmonic materials have been used as a component of photocatalysts.

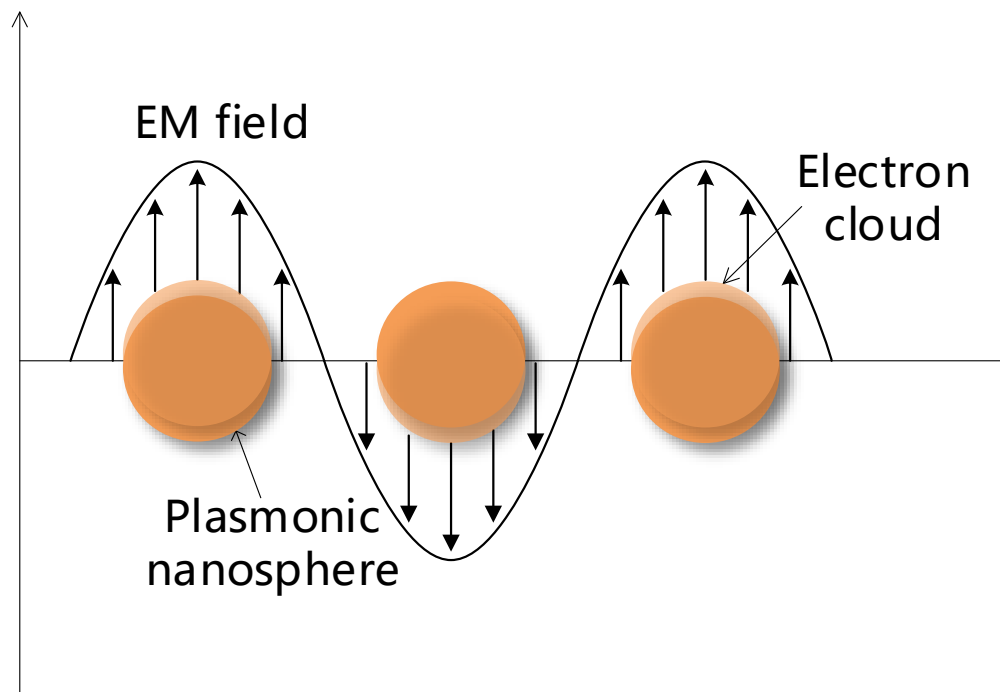


**Figure 1.** Schematic illustration of LSPR for a plasmonic nanosphere [7].

Among plasmonic materials, the high free carrier density of noble metal NPs makes their LSPR frequencies always in the visible or near-infrared region [5], along with a good chemical stability, so noble-metal-based photocatalysts have received wide attention for their photocatalytic performance and application potential, such as Ag-based and Au-based photocatalysts. Plasmonic noble metals are often introduced into the modification process of semiconductor photocatalysts to form composite photocatalysts to improve their photocatalytic performance [9], such as some two-component composite materials, such as Ag/AgX (X = Cl, Br, I) [10–12], Ag/TiO<sub>2</sub> [13], Ag/MoO<sub>3</sub> [14], Au/g-C<sub>3</sub>N<sub>4</sub> [15], and Au/TiO<sub>2</sub> [16], and even three-component composite materials, such as Ag-AgI-Bi<sub>5</sub>O<sub>7</sub>I [17], Ag/AgCl-CdWO<sub>4</sub> [18], Ag/AgBr/MoO<sub>3</sub> [19], and Ag/Ag<sub>2</sub>CO<sub>3</sub>-rGO [20]. In these noble-metal-based photocatalysts, when SPR is triggered, a strong inhomogeneous electromagnetic (EM) field is generated near the metal nanoparticles, and the energy stored in the surface plasma is transferred to the semiconductor compounded with the noble metal through the plasmon-induced resonance energy transfer (PRET) process, which greatly stimulates the nearby semiconductor and contributes to the reduction in optical carrier recombination while broadening the light response range of the material. Hot electron injection is also present in noble-metal-based photocatalytic systems, where electron–electron and electron–phonon interactions generate hot electrons during plasma decay, affecting subsequent chemical reactions. The metallic properties of metals can also be used as electron donors to increase the photogenerated carriers in the photocatalytic process to drive the photocatalytic reaction, and the photothermal and catalytic effects of metals also promote the photocatalytic reaction [21]. Some researchers have even prepared new plasmonic p–n heterojunction photocatalysts by combining the p–n heterojunction structure with plasmonic noble metals. Experimental results show that the photocatalytic performance of the new composite photocatalysts is better than that of single p–n heterojunction photocatalysts. In the new plasmonic p–n heterojunction photocatalysts, the p–n heterojunction can suppress charge

complexation, and the SPR effect of noble metals can enhance the absorption of visible light [22–25]. These precious-metal-based photocatalysts with LSPR effects currently have applications in environmental remediation, energy conversion, and medical science [26–28].

In general, the addition of these noble metals broadens the optical response range of semiconductors, improves the carrier separation efficiency, and effectively increases the photocatalytic activity, but there are still limitations in the practical application of noble metal NPs in photocatalysis due to their high cost, high optical loss, fixed plasma frequency, and low abundance [6]. LSPR is not limited to noble metal NPs; some other materials with a large number of free carriers can also undergo SPR. LSPRs have also been discovered in some non-noble metals, such as Bi [29–49], Cu [50–65], Al [66–73], and Zn [74]. Except metal NPs, LSPRs can also occur on some heavily doped semiconductors and metal oxides with a lower free carrier density than noble metals [6,75–109].

There are many reviews in the literature on the experimental preparation of noble-metal-based plasmonic photocatalysts [110] or on the energy transfer mechanism of plasmonic photocatalysts, but few reviews exist on non-noble metal and nonmetallic plasmonic photocatalysts [111]. In this review, we review the types, properties, advantages and disadvantages, experimental preparation, applications, and their photocatalytic mechanisms of non-noble metal and nonmetallic plasmonic photocatalysts, and finally we provide an outlook on non-noble metal and nonmetallic plasmonic photocatalysts to achieve a superior photocatalytic performance to solve environmental problems and energy shortages.

## 2. Non-Noble Metal Plasmonic Nanomaterials

Non-noble metal plasmonic nanomaterials arouse attention in the field of photocatalyst with LSPRs which can broaden the absorption light range of the photocatalysts, improve the effective separation and migration of light-generated carriers, and reduce the recombination rate of electron–hole pairs, such as Bi [29–49], Cu [50–65], Al [66–73], and Ni [112–115], and some other non-noble metals that also possess plasmonic behavior include Zn [74], Na [116], Mg [117–119], Ga [120,121], In [120], etc. In building photocatalysts, researchers often add non-noble metal plasmonic nanomaterials in combination with other semiconductors to improve the overall photocatalytic performance of the photocatalyst by exploiting its LSPRs and metallic properties. Among the non-noble metals found to possess plasmonic properties, the most common to occur in photocatalytic systems are Bi, Cu, and Al. This section will also illustrate the application and exploration possibilities of non-noble metal plasmonic nanomaterials in photocatalysis by focusing on the plasmonic properties, advantages, disadvantages, and applications of Bi, Cu, Al, and Ni.

### 2.1. Bi-Based Composite Photocatalysts

Bismuth is an earth-abundant metalloid with a very narrow band gap, a much lower cost than noble metals, and a highly anisotropic Fermi surface, but with poor photocatalytic activity [29,30,33]. Bi NPs are good direct plasma photocatalysts. Pure Bi NPs are rapidly oxidized in air, and the hot carriers generated by Bi through SPR are easily deactivated, so Bi NPs often need to be coupled with semiconductors or carriers that accept hot electrons generated by Bi to prevent deactivation [45]. Selecting a material to protect the surface of Bi NPs to keep the purity of Bi NPs is further demanded for its improvement of photocatalysis [29]. In Yawen Li's research, Bi NPs were acquired via a liquid phase chemical reduction method, and then Bi@SiO<sub>2</sub> NPs were synthesized by designing a thin SiO<sub>2</sub> layer on the Bi NPs to prevent Bi from oxidation. It can be found that the composite material belongs to a core–shell structure by various characterizations in their work. The SPR and light scattering of Bi allows the material to have a wide and strong light absorption in the visible range. The addition of the SiO<sub>2</sub> layer has no effect on the optical properties of Bi NPs and, as an isolated shell layer, it increases the local refractive index around Bi NPs, which promotes the LSPR of Bi, while the porous structure of the material contributes to the separation of light-generated electron holes by trapping and transferring electrons. However, the excessively thick SiO<sub>2</sub> shell also affects the free transfer of hot electrons and thus the photocatalytic

performance. The experiments demonstrate that the composite has strong photocatalytic activity for the degradation of rhodamine B (RhB) and bisphenol A (BPA) [29]. Plasmonic Bi NPs usually form composite photocatalysts with semiconductors to exploit the SPR effect of Bi NPs, thereby improving the semiconductors' photocatalytic performance, such as Bi-NPs@GO [30], C/Bi/Bi<sub>2</sub>O<sub>3</sub> [31], Bi/Bi<sub>2</sub>O<sub>3</sub>@C [32], Bi/Bi<sub>2</sub>WO<sub>6</sub> [33], g-C<sub>3</sub>N<sub>4</sub>@Bi@Bi<sub>2</sub>WO<sub>6</sub> [34], Bi@Bi<sub>5</sub>O<sub>7</sub>I/rGO [35], Bi NPs/BiOCl/ZnSn(OH)<sub>6</sub> [36], Bi/(BiO)<sub>2</sub>CO<sub>3</sub> [41], BC/Bi/Fe<sub>3</sub>O<sub>4</sub> [43], and Cu<sub>2</sub>O/Bi/Bi<sub>2</sub>MoO<sub>6</sub> [44]. In the composite photocatalytic material system composed of Bi NPs and semiconductor, the SPR of Bi NPs enhances the absorption of visible light, and its induced electric field can promote the segregation of photogenerated electrons and holes. Bi NPs may play three main roles in improving the photocatalytic performance of photocatalyst: (i) After coupling to a semiconductor with a matched band gap structure, the thermal electrons generated by Bi through SPR can be transferred to conduction band (CB) of the semiconductor under light irradiation to participate in the subsequent chemical reaction [43] (Figure 2a); (ii) Bi can be used as an electron acceptor or hole trap to accept electrons from the semiconductor CB to promote the separation of photogenerated carriers [42,47] (Figure 2b); and (iii) Bi NPs can be used as a charge transfer medium between different semiconductors to transfer photogenerated electrons from CB of one semiconductor to the CB or valence band (VB) of another semiconductor to promote the segregation of photogenerated carriers in the whole photocatalyst system [37,44,48] (Figure 2c). Some Bi NP semiconductor composite materials in which the Bi metal work as a cocatalyst can improve their photocatalytic activity attributed to the co-effects of LSPRs of Bi NPs and other effects of some special structures, such as the heterostructure or oxygen vacancies. A unique core/shell Bi<sub>4</sub>MoO<sub>9</sub>/Bi<sup>0</sup> heterostructure photocatalyst with an abundance of oxygen vacancies has been synthesized. This photocatalyst performs excellent photocatalytic NO removal under visible light irradiation compared with pristine Bi<sub>4</sub>MoO<sub>9</sub> thanks to the cooperative effect of the LSPRs of the Bi and Bi<sub>4</sub>MoO<sub>9</sub>/Bi<sup>0</sup> heterojunction [38]. LSPRs can enhance visible light absorption and reduce the recombination of photogenerated electron–hole pairs, while Bi<sub>4</sub>MoO<sub>9</sub>/Bi<sup>0</sup> heterojunctions can effectively direct an electron transfer between the two components to promote electron–hole separation, and oxygen-vacancy-induced defect states allow more electrons to overcome the wide band gap and transfer from the VB to the CB, generating more active species [38]. In previous studies, the most common synthesis method for metallic Bi used was chemical reduction synthesis via a solvothermal reaction, and the composition, proportion [29], and structure [36] of a Bi-based composite photocatalyst can affect its photocatalytic performance; therefore, we can regulate these issues via different methods to achieve a higher photocatalytic activity in further work. The detailed photocatalytic performances of non-noble-plasmonic-metal-Bi-nanomaterials-based photocatalysts are shown in Table 1.

## 2.2. Cu-Based Photocatalysts

Similarly, as non-noble metals materials, copper (Cu) also has SPRs, and they can also improve photocatalytic ability by collecting low-energy photons in visible and even infrared regions, thus expanding the field of light sorption and improving the carrier separation efficiency. Therefore, Cu-based photocatalytic materials have been studied more in the field of plasma photocatalysis.

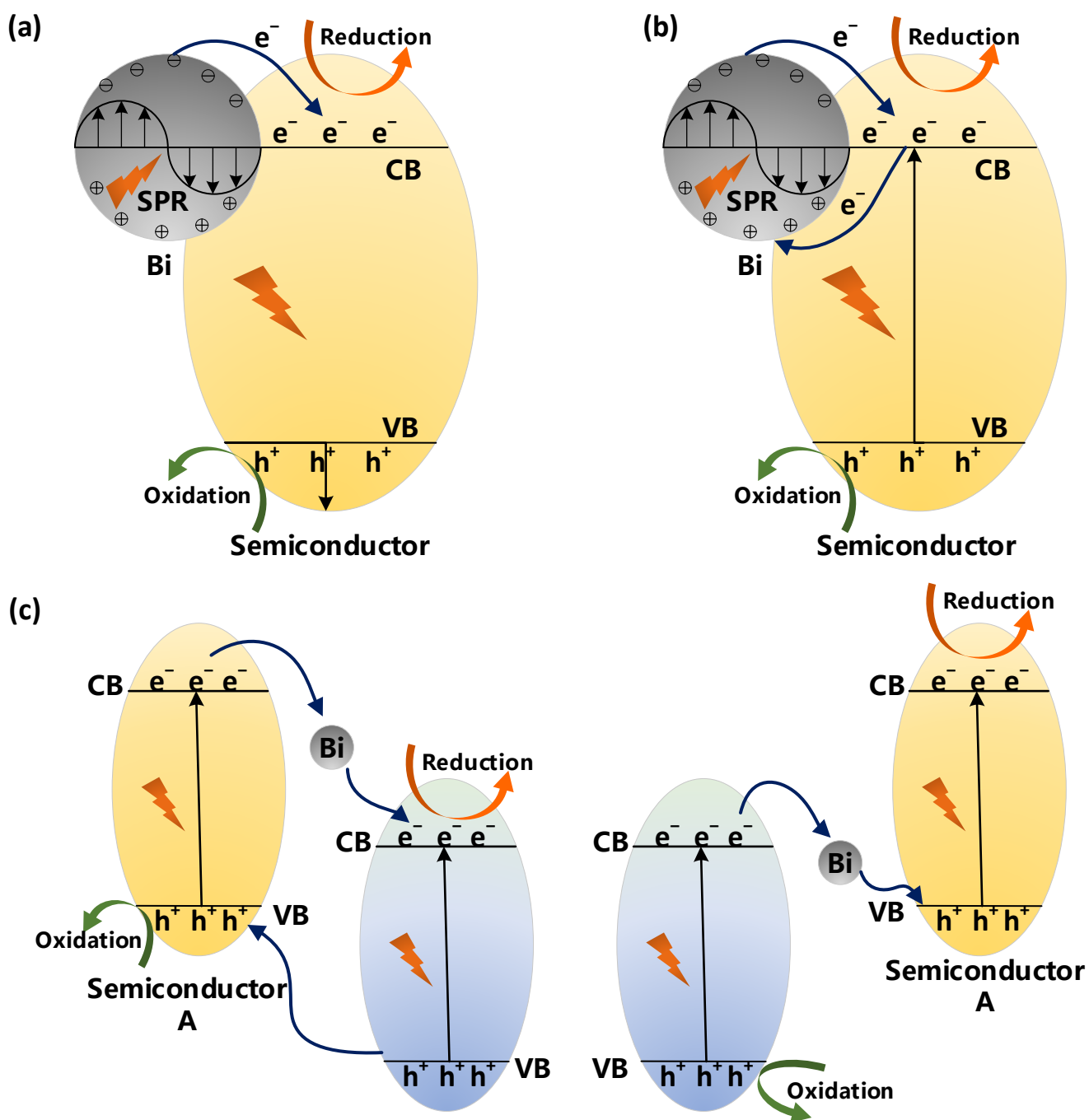


**Figure 2.** Photocatalytic mechanism of Bi-based composite photocatalysts with the light illumination [37,42–44,47,48]. After coupling to a semiconductor with a matched band gap structure, the thermal electrons generated by Bi through SPR can be transferred to conduction band (CB) of the semi-conductor under light irradiation to participate in the subsequent chemical reaction (a); b: Bi can be used as an electron acceptor or hole trap to accept electrons from the semiconductor CB to promote the separation of photogenerated carriers (b); Bi NPs can be used as a charge transfer medium between different semiconductors to transfer photogenerated electrons from CB of one semiconductor to the CB or valence band (VB) of another semiconductor to promote the segregation of photogenerated carriers in the whole photocatalyst system (c).

**Table 1.** Summary of photocatalytic performances of plasmonic-Bi-nanomaterials-based photocatalysts.

Materials	Preparation Method	Origin of LSPR	Structure	Light Source	Objects	Efficiency	Ref.
Bi@SiO <sub>2</sub> (Bi:SiO <sub>2</sub> = 1:0.1)	Liquid phase chemical reduction method	Bi	Core-shell	Iodine lamp	RhB(10 ppm) BPA(20 ppm)	Degradation, 44.35% in 60 min Degradation, 49.10% in 60 min	[29]
Bi@SiO <sub>2</sub> (Bi:SiO <sub>2</sub> = 1:0.3)					RhB(10 ppm) BPA(20 ppm)	Degradation, 63.32% in 60 min Degradation, 40.0% in 60 min	
Bi-NPs@GO	A solution-based sonication method	Bi	Sphere	UV lamp	NO(100 ppm)	Removal, 42.3% in 30 min	[30]
C/Bi/Bi <sub>2</sub> O <sub>3</sub>	One-pot method	Bi	—	Xe lamp (visible light + simulated sunlight)	2,4-DCP(10 mg/L)	—	[31]
Bi <sup>o</sup> /Bi <sub>2</sub> O <sub>3</sub> @C	A surfactant-assisted sol-gel method	Bi	—	LED daylight bulb	MB(10 mg/L)	Degradation, 75.0% in 60 min	[32]
Bi/Bi <sub>2</sub> WO <sub>6</sub>	Hydrothermal reaction + solvothermal method	Bi	Hierarchical architecture	Visible light	RhB(10 mg/L) 4-CP(20 mg/L)	Degradation, 93.0% in 25 min Degradation, 54.4% in 120 min	[33]
g-C <sub>3</sub> N <sub>4</sub> @Bi@Bi <sub>2</sub> WO <sub>6</sub>	Hydrothermal method	Bi	Flower-like hierarchical microspheres	Xe lamp	MO(10 mg/L) RhB(20 mg/L)	Degradation, 70% in 120 min Degradation, 100% in 30 min	[34]
					2,4-DCP(20 mg/L)	Degradation, 72% in 180 min	
Bi@Bi <sub>4</sub> O <sub>7</sub> I/rGO	Surface-charge-mediated self-assembly strategy	Bi	2D nanosheet	Visible light	LVFX(20 mg/L)	Degradation, 45.24% in 120 min	[35]
Bi NPs/BiOCl/ZnSn(OH) <sub>6</sub> (ZSH-1-Bi)	One-pot precipitation, hydrolysis, and UV-photoreduction process	Bi	Cubes	Visible light	RhB (48 mg/L)	Degradation, 83.5% in 120 min	[36]
Bi NPs/BiOCl/ZnSn(OH) <sub>6</sub> (ZSH-2-Bi)			14-facets polyhedron			Degradation, 65.6% in 120 min	
Bi NPs/BiOCl/ZnSn(OH) <sub>6</sub> (ZSH-3-Bi)			Octahedron			Degradation, 91.4% in 120 min	
Bi <sub>4</sub> MoO <sub>9</sub> /Bi <sup>o</sup>	Hydrothermal method	Bi	Core-shell	Tungsten halogen lamp	NO(100 ppm)	Removal, 57.2%	[38]
Bi@BiOCl	One-step solvothermal method	Bi	Hierarchical microsphere	Tungsten halogen lamp	NO(100 ppm)	Removal, 67.5%	[39]
Bi-Bi <sub>2</sub> S <sub>3</sub> -g-C <sub>3</sub> N <sub>4</sub>	Solvothermal method	Bi	PG structure	Visible light	Cr(VI) (20 mg/L) TC(10 mg/L)	Removal, 0.03921 min <sup>-1</sup> Degradation, 92.5% in 150 min	[40]
Bi/(BiO) <sub>2</sub> CO <sub>3</sub>	—	Bi	Stacked irregular nanoplates	Tungsten halogen lamp	NO(100 ppm)	Removal, 63.6% in 30 min	[41]
BC/Bi/Fe <sub>3</sub> O <sub>4</sub>	High-temperature calcination	Bi	The rod covered with nanoparticles	Xe lamp	Cr(VI) (20 mg/L)	Removal, 95% in 180 min	[43]
Cu <sub>2</sub> O/Bi/Bi <sub>2</sub> MoO <sub>6</sub>	Two-step hydrothermal route + wet-impregnation	Bi	—	Visible light	Sulfadiazine (10 mg/L) Ni(II)(10 mg/L)	Degradation, 98.6% in 100 min Degradation, 93.2% in 60 min	[44]
g-C <sub>3</sub> N <sub>4</sub> /Bi/Bi <sub>3.64</sub> Mo <sub>0.36</sub> O <sub>6.55</sub>	In situ reduction technique	Bi	—	Xe lamp	lomefloxacin (10 mg/L)	Degradation, 94.6% in 20 min	[48]

Compared with Au and Ag, Cu has a comparable visible LSPR effect and even a strong LSPR response in the NIR. However, Cu has a much lower cost and higher natural abundance than Ag and Au and has a high electrical conductivity and high thermal conductivity [59]. With the same disadvantages as Bi metal, Cu metal materials have a poor chemical stability and are easy to be oxidized and to reunite, so the development of pure Cu NPs as a direct photocatalyst is limited [50,51]. Cu is easily oxidized in the environment, and O<sub>2</sub> or even H<sub>2</sub>O can easily oxidize Cu nanomaterials. However, when Cu NPs contain a large amount of Cu<sub>2</sub>O, the photocatalytic activity will be reduced [59,63]. Therefore, combining Cu NPs with other photocatalytic materials to synthesize photocatalysts and improve the photocatalytic performance by tuning the composition and proportion, size, and morphology can be the further development direction of Cu-based photocatalytic materials [52]. In Benlin Dai's study, different ratios of Cu@Cu<sub>2</sub>O samples were prepared for the photocatalytic reduction of CO<sub>2</sub> and photocatalytic oxidation of NO by the in-situ

generation of Cu NPs on the octahedral surface of Cu<sub>2</sub>O by chemical reduction. It was found that the photocatalytic properties of the samples could be improved by adjusting the Cu content in the Cu@Cu<sub>2</sub>O samples, but excessive Cu NPs would also be more likely to cause photogenerated electron and hole recombination, thus reducing the photocatalytic performance of the samples [65]. In a large number of studies on plasmonic Cu NPs, Cu NPs are usually combined with some semiconductor materials or some other materials that behave similarly to semiconductors to form composite photocatalysts, thus taking advantage of their excellent properties and some synergistic effects to improve the defects which exist when they are used as photocatalysts alone, protect Cu from the environment, and at the same time increase the transfer efficiency of light-borne carriers, and greatly improve the photocatalytic activity and long-term catalytic stability of the materials, such as Cu/graphene [50], Cu/TiO<sub>2</sub> [52], Cu/Cu<sub>2</sub>O/TiO<sub>2</sub> [53], Cu UiO-66 [54], Cu/rGO [55], and Cu@Cu<sub>2</sub>O/SiO<sub>2</sub> [57]. The detailed photocatalytic performance of Cu-based materials is listed in Table 2.

**Table 2.** Summary of photocatalytic performances of non-noble-plasmonic-metal-Cu-nanomaterials-based photocatalysts.

Materials	Preparation Method	Origin of LSPR	Structure	Light Source	Objects	Efficiency	Ref.
Cu/graphene (Cu/CG-1100)	In situ synthesis method	Cu	Stacked layers of nanosheets	Xe lamp	H <sub>2</sub>	Evolution, 3.94 mmol·g <sup>-1</sup> ·h <sup>-1</sup>	[50]
CuCo	Hydrothermal method	Cu	Dendrite-like	Xe lamp	H <sub>2</sub>	Evolution, 77.1 μmol·g <sup>-1</sup> ·h <sup>-1</sup>	[51]
Cu/TiO <sub>2</sub>	Hydrothermal method	Cu	Nanorods	UVA lamps	CO <sub>2</sub>	Reduction, 2.91 ppm/g <sub>catal</sub>	[52]
Cu film/Cu <sub>2</sub> O/TiNT	Anodization combined with electrodeposition method	Cu	—	Xe lamp	MB(10 mg/L)	Degradation, 100% in 30 min	[53]
Cu/UiO-66	Double-solvent approach + one-step reduction	Cu	Octahedrons	Xe lamp	Benzyl alcohol	Oxidation, 53.3%	[54]
Cu/rGO	In situ photoreduction process	Cu	Nanosheets	Xe lamp	H <sub>2</sub>	Evolution, 59 mmol·g <sup>-1</sup> ·h <sup>-1</sup>	[55]
Cu@Cu <sub>2</sub> O/SiO <sub>2</sub>	Precipitation and sol-gel methods	Cu	Cubic shapes	Sunlight	CIP(2 mg/L)	Degradation, 94.24% in 60 min	[57]

In another case, other metals and Cu were introduced to form bimetallic or poly-metallic photocatalysts, and the introduced foreign metals were used as adsorption and activation centers for the reactants, which greatly improves the charge transfer efficiency and prevents the direct recombination of light-induced electron–hole pairs caused by SPR on Cu NPs [58,61,62,64]. In Zhang’s research, a plasmonic non-semiconductor photocatalyst was synthesized for effective hydrogen evolution and storage, and the prepared dendrite-like plasmonic metal Cu had the SPRs in photocatalytic water splitting to generate H<sub>2</sub>. By designing CuCo bimetal via a hydrothermal method and controlling the proportion of Cu and Co and the preparation temperature, a 3.5-fold time improvement for H<sub>2</sub> evolution compared to the Cu has been achieved with a proportion of 7:3 and a preparation temperature of 200 °C [51]. In this photocatalyst system, the SPR effect of Cu, the enlarged surface area, and promotion of the charge separation and transferring due to the growth of the Co nanosheets on the surface of Cu means there is an outstanding H<sub>2</sub> evolution–storage integration of the CuCo bimetal photocatalyst at room temperature [51].

Cu can also form core–shell structures with metal oxides such as graphene to protect it from environmental effects [58]. Cu is readily oxidized in the environment to form Cu<sub>2</sub>O, but it has been proved that there is an optimal covering thickness of Cu<sub>2</sub>O that causes the LSPR absorption peak of Cu NPs to redshift. Therefore, Cu NPs can be oxidized to prepare Cu@Cu<sub>2</sub>O and absorb NIR light, and Cu<sub>2</sub>O can also be used to separate thermal electrons generated by Cu nuclei, greatly improving the solar energy conversion efficiency [60].

Like Bi NPs, the addition of Cu NPs with the LSPR effect can enhance the photocatalytic properties of the whole photocatalyst system. However, as a photocatalytic material, Cu cannot be synthesized on a large scale due to the difficulty of reducing the copper precursor to the metal state, which also limits its application.

### 2.3. Al-Based Photocatalysts

Al is the most plentiful metallic element in the Earth's crust and is a promising plasma metal. Al has a wide plasma band, and the LSPR frequency of Al can be tuned from UV to NIR by changing the size and shape of Al NPs [69,71]. Liu et al. [73] discussed the influence of Al size and the ratio of Al to TiO<sub>2</sub> on the photocatalytic degradation of methylene blue by Al/TiO<sub>2</sub> and found that the size of the Al particle would affect the wavelength range of the LSPR effect, and the larger the Al particle, the stronger the light absorption, but when the size is too large, most of extinction scattering will be caused, and the electron oscillation cannot be excited. At the same time, appropriately increasing the ratio of Al to TiO<sub>2</sub> can effectively improve the photocatalytic efficiency. Al is also prone to oxidation as the same as Bi and Cu, and the Al<sub>2</sub>O<sub>3</sub> layer is often formed on the surface of Al NPs, and this Al<sub>2</sub>O<sub>3</sub> layer can provide adsorption sites [71]. Al NPs can also be a co-catalyst or be a candidate in some photocatalytic systems to improve the photocatalytic performance [66,72]. In the course of the study of Qi Hao, plasmonic Al nano-void arrays have been fabricated with tunable LSPR energies to overlap the plasmonic spectrum and TiO<sub>2</sub> bandgap. The degradation rate of RhB by the TiO<sub>2</sub>/Al photocatalyst is very high due to coupling between Al and TiO<sub>2</sub>, which includes the LSPR effect through radiative energy transfer when the Al plasmonic band is coupled with the TiO<sub>2</sub> band gap and the photocatalysis caused by the interfacial charge transfer process at the TiO<sub>2</sub>/Al interface, which is independent of the Al<sub>2</sub>O<sub>3</sub> layer on the surface [66]. Al NPs can be combined with conventional catalytic materials to form an "antennae-reactor" complex, which focuses light on the catalytic reactor and couples LSPR energy to a poorly absorbent photocatalyst through near-field interaction, effectively generating hot carriers and converting the entire nanostructure into a photocatalyst, such as coupling Al and Pd, which can effectively improve the interaction of Pd with light and promote photocatalytic hydrolysis [67,70].

Al NPs produce the strong absorption of incident light when the incident light frequency is the same as the frequency of free electrons on the metal surface, when the surface free electrons undergo collective oscillation and a very strong electric field is generated around them, which is the LSPRs of Al NPs. When Al NPs are combined with other semiconductor materials, the high EM and PRET can greatly excite the surrounding semiconductor and enhance the light absorption of the semiconductor, while the generation of hot electrons during the plasma decay process increases the free carrier concentration, and Al NPs can also act as electron acceptors to enable the effective segregation of semiconductor light-generated carriers. As with Bi NPs and Cu NPs, the addition of Al NPs can enhance the photocatalytic properties of the whole photocatalyst system.

### 2.4. Ni-Based Photocatalysts

Nickel (Ni) is an earth-abundant and stable transition metal that is commonly used in batteries, coins, and catalysts. Ni, as a non-precious plasma metal, has been relatively little studied, but some researchers have applied Ni NPs with plasma effects in photocatalysis to enhance photocatalytic performance. Hao et al. [112] synthesized  $\beta$ -Bi<sub>2</sub>O<sub>3</sub>-NiO/Ni heterojunction photocatalysts using a one-step combustion method, which exhibited the superior visible light photodegradation of the dyes MB and RhB. In the catalyst system, the metal Ni exhibited a plasmonic effect and the presence of Ni increased the light absorption of the NiO/Ni material, but the photoinduced electron and hole binding of NiO/Ni was faster and the photocatalytic activity was low. When it was coupled with  $\beta$ -Bi<sub>2</sub>O<sub>3</sub> to form a heterojunction photocatalyst, electrons could migrate from the CB of NiO/Ni to CB of  $\beta$ -Bi<sub>2</sub>O<sub>3</sub> and holes could migrate from VB of  $\beta$ -Bi<sub>2</sub>O<sub>3</sub> to VB of NiO/Ni, which inhibits the compounding of electron-hole pairs on NiO/Ni and greatly improves the photocatalytic activity of the material. Similarly, in Talebi's study, different sizes and compositions of Ni@NiO/NiCO<sub>3</sub> core-shell was used for photocatalytic hydrogen production and the UV-Vis absorbance spectroscopy results of the samples indicated a broad peak at 470 nm, which was attributed to the SPR of Ni NPs, while there was no corresponding absorption peak/edge for NiO, indicating plasma-driven H<sub>2</sub> evolution. Under light irradiation, Ni par-

ticles generate hot electrons through the SPR effect, plasma electrons from Ni are transferred to NiCO<sub>3</sub> via NiO, and the NiO/NiCO<sub>3</sub> shell layer acts as a dielectric layer to promote plasma generation on the surface of the Ni NPs [114]. When semiconductor materials alone are used for photocatalysis, disadvantages such as poor light absorption and rapid photoexcited carrier recombination make photocatalysis limited. Therefore, plasma metals can be introduced to create heterojunctions to effectively overcome the limitations, broaden the light absorption of semiconductor materials, and inhibit photo-generated carrier recombination, thus improving the photocatalytic activity. Ullah et al. [115] doped metal Ni NPs into semiconductor g-C<sub>3</sub>N<sub>4</sub> to form a heterojunction photocatalyst g-C<sub>3</sub>N<sub>4</sub>/Ni@N-doped C. Under visible light irradiation, the Ni NPs have strong surface plasma absorption, and the excited Ni NPs generate a large amount of surface plasma and decay rapidly to produce hot electrons, which jump above the Fermi energy level of Ni, and due to SPR, the plasma hot electrons are transported to the CB of g-C<sub>3</sub>N<sub>4</sub> that participates in the subsequent H<sub>2</sub> evolution [115]. The addition of Ni NPs with the LSPR effect can improve the photocatalytic performance of the whole photocatalytic system. At present, there are relatively few studies on the use of plasmonic metal Ni NPs for photocatalysis and their applications, and more consideration can be given to the possibilities of Ni NPs in the field of photocatalysis in the future.

### 3. Nonmetallic Plasmonic Nanomaterials

In addition to the noble metal and non-noble metal plasmonic nanomaterials, LSPRs also can be discovered in some metal oxide nanocrystals and other semiconductors which have abundant free carriers, including free electrons and holes aroused by doping. In contrast, the free carrier density in heavily doped semiconductors is lower than that in plasmonic noble metals so that their LSPR frequencies are at longer wavelengths. In the preparation of nonmetallic plasmonic nanomaterials, the LSPR frequency can be tuned by controlling the dopant concentration, changing the stoichiometric compositions and phase changes, but the LSPR frequencies of noble metals are fixed [5,6,80]. To achieve different LSPR frequencies in UV-NIR-MIR regions to meet different needs and lower cost, some plasmonic metal oxide and other semiconductors photocatalysts have been studied [5,6,74–102,106,107,109,122–128]. Nonmetallic [122,123] plasmonic nanomaterials can be divided into two categories: extrinsic doping nanomaterials which are doped with heterovalent, and self-doped nanomaterials with deficient cation or anion vacancies by intrinsic formation [5]. In addition to these, TiN is also a typical non-metallic plasma material with a nice LSPR effect and a wide light absorption in the range of 500 to 1200 nm, a broad plasma resonance which ranges from visible to near-infrared [129,130].

Nonmetallic plasmonic nanomaterials have an important advantage of integrating metallic LSPRs with the properties of semiconductors themselves, which cannot only take advantage of metal LSPR, but also use doping, heterojunctions, and co-catalysts, etc., to overcome their own instability, low carrier concentration, and high electron–hole recombination rate, and can also control the free carrier concentration by controlling the composition and concentration of the host material and dopant, so that the LSPR frequency can be tuned.

#### 3.1. Extrinsic Doping Metal Oxides/Semiconductors

Doping heterovalent atoms can achieve a high density of free carriers to support LSPR. Metal oxides are wide-gap semiconductors, and their energy usually falls in the visible or near-UV spectrum. However, controlling the doping of these materials via the introduction of vacancies, interstitial atoms, or aliovalent substitutional impurities can yield the sufficient concentration of free carriers to support LSPR [108]. Metal oxides doped with heterovalent atoms mainly involve Sn-doped In<sub>2</sub>O<sub>3</sub> (ITO) [6,77–79], Al-doped ZnO (AZO) [80–82], Sb-doped SnO<sub>2</sub> [81], In-doped CdO [83,84], and Ne-doped TiO<sub>2</sub> [5]. ITO NCs with wider LSPR frequencies in NIR and mid-infrared (MIR) regions were achieved via a solvothermal synthesis method. By doping Sn, ITO NCs exhibit good electrical

conductivity and optical characteristics, thus facilitating the application of ITO NCs in NIR and MIR regions. The LSPR frequencies changed regularly in three stages, which was attributed to the amount of Sn and the Sn potential synergistic effect of the trapping ability. In the first stage, LSPR frequencies shifted gradually toward shorter wavelengths with the increasing ratios of Sn. In the next stage, with the further increasing amount of Sn, the position of LSPR shifted towards longer wavelengths. In the last stage, the LSPR frequency shifted to the shorter wavelength again [6]. Additionally, as an extrinsic doping metal oxide, AZO, which was synthesized via atomic layer deposition, was studied. It showed that a simple protection layer and thermal treatment can be used to reduce the optical loss of the films and convert a crossover wavelength to near-infrared wavelengths, and the enhanced optical properties, owing to the migration and subsequent activation of doped Al in the ZnO matrix, are allowed. Moreover, the use of a HfO<sub>2</sub> protection layer prevents the formation of defects. Meanwhile, the fact that the LSPR mode is highly tunable by varying the doping concentration, heat treatment time, deposition temperature, and ZnO buffer thickness has been verified [80]. By introducing Er<sup>3+</sup> into CuS, the band gap and defects of the photocatalysts were changed, and LSPR caused by the free holes in the valence band was tuned. Additionally, the photocatalytic performance of Er:CuS was enhanced due to the surface defect and Cu vacancies which can suppress the photogenerated electron–hole recombination [109]. All of these studies show that the doping concentration affects the LSPR effect of the photocatalysts system, and a different LSPR frequency can be achieved by tuning the dopant concentration.

### 3.2. Self-Doped Metal Oxides/Semiconductors

Self-doped metal oxides or other semiconductors could support LSPR with a high enough density of free carriers due to the deficiencies. The main materials include copper-deficient chalcogenides (Cu<sub>2-x</sub>E, E = S, Te, Se) [76,85–91], MoS<sub>2-x</sub> and oxygen-deficient transition metal oxides, including TiO<sub>2-x</sub>, WO<sub>3-x</sub> [75,92–96,126–128], MoO<sub>3-x</sub> [97–105,125], and ZnO [106,107].

Cu<sub>2-x</sub>S as a nonstoichiometric semiconductor shows good plasmonic adsorption in the NIR region owing to the high density of holes in the valence band aroused by the Cu deficiencies. The wavelength of the LSPR can be easily changed by modifying the number of vacancies in the VB [90]. The semiconductor with the LSPR effect is compounded with other semiconductors to form a heterogeneous junction and other structures, which can promote the widening of the light absorption range of materials and the improvement of the carrier separation efficiency, such as ternary sulfide ZnS-CdS-Cu<sub>2-x</sub>S. In Zhuang's research, these heterojunction materials achieve nearly full spectrum absorption, including NIR absorption (Cu<sub>2-x</sub>S), visible absorption (CdS), and UV absorption (ZnS). The p-n heterojunctions between CdS and Cu<sub>2-x</sub>S enhance the separation efficiency of the photogenerated electrons and holes so that a large number of holes were collected in the semiconductor VB and the LSPR effect is facilitated and optical properties can be improved compared to binary ZnS-CdS and bare ZnS [76]. The reaction time, temperature, and concentration of diphenyl phosphine (DPP) are important parameters to regulate the size and shape of Cu<sub>2-x</sub>Te NPs during a preparation process with the presence of DPP, which can facilitate the anisotropic growth of the formation of cubic structures with better NIR adsorption due to the LSPR effect which is aroused by Cu deficiencies [86]. In plasmonic Cu<sub>2-x</sub>Se@ZnS core shell NPs, the ZnS shell can prevent the oxidation of the Cu<sub>2-x</sub>Se core in a strongly reducing environment, but a slow oxidation still occurred due to the diffusion of the Cu<sup>+</sup> through ZnS, and this can achieve an LSPR effect in the NIR region owing to the Cu vacancies, so we can also tune the LSPR by the oxidative treatment of the particles [85]. All of these show that the composition, shape, and structures of Cu<sub>2-x</sub>E (E = S, Te, Se) and the co-effect with other semiconductors can affect its LSPR effect and the optical properties.

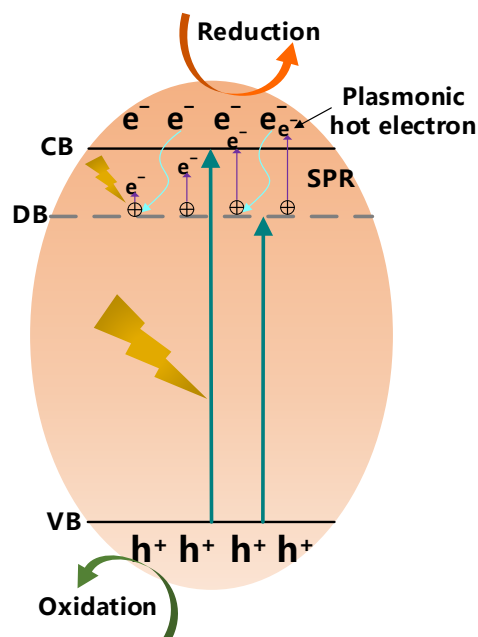
Oxygen vacancy defects are important to enhance the light capturing and photocatalytic activities of metal oxides, with the absorption light region extending into the NIR due to the LSPR effect, such as non-stoichiometric metal oxides WO<sub>3-x</sub> [75,92–96,126–128],

TiO<sub>2-x</sub>, MoO<sub>3-x</sub> [97–105,125], and ZnO [106,107]. With the advantages of powerful oxidation properties, low cost, and non-toxicity, WO<sub>3</sub> can be modified by various methods to improve its photocatalytic activity. By introducing oxygen vacancies, the photocatalytic performance of WO<sub>3</sub> can be enhanced greatly and its absorption of visible light and conductivity can be increased by the LSPR effect of WO<sub>3-x</sub> in the NIR region. Introducing oxygen vacancy through low temperature annealing in alcohol to WO<sub>3</sub> to obtain non-stoichiometric metal oxides WO<sub>3-x</sub> can achieve a high concentration of oxygen vacancies which act as traps to reduce the recombination of photogenerated electron–hole pairs and improve the separation efficiency of free carriers and improve their photocatalytic performance [92]. The stability of W<sub>18</sub>O<sub>49</sub> is better than that of WO<sub>3</sub> [128]. This is because the LSPR of W<sub>18</sub>O<sub>49</sub> derives from the localized electron confinement around lattice W<sup>5+</sup>-W<sup>5+</sup> in the unique structure of W<sub>18</sub>O<sub>49</sub>, which makes W<sub>18</sub>O<sub>49</sub> have a wide absorption from visible light to NIR, independent of the particle shape and size. Therefore, the NIR absorption of W<sub>18</sub>O<sub>49</sub> is an inherent property, while that of WO<sub>3</sub> depends on oxygen vacancy, which varies greatly under light [128]. At the same time, under visible light irradiation, oxygen-vacancy-induced free electrons are excited by LSPR to become thermal electrons, enhancing photocatalysis [95,96]. However, a single semiconductor with oxygen vacancies is too difficult to obtain an excellent photocatalytic performance and achieve more stringent requirements such as adsorbing light across the whole solar spectrum and generating active charge carriers on suitable levels for generating or degrading target materials by using LSPR-excited “hot electrons” [94]. Therefore, some composite photocatalytic materials based on WO<sub>3-x</sub> have been developed [75,93,94,126–128]. A plasmonic Z-Scheme photocatalyst with the W<sub>18</sub>O<sub>49</sub>/g-C<sub>3</sub>N<sub>4</sub> heterostructure is presented. The synergistic effect of LSPR absorption of W<sub>18</sub>O<sub>49</sub> in the visible and NIR region to induce a “hot electrons” injection process and Z-scheme-improved charge carriers’ separation enhances the photocatalytic efficiency of H<sub>2</sub> evolution [93]. MoO<sub>3</sub> is also a non-toxic, low-cost semiconductor material with an excellent adsorption capacity [97]. When oxygen vacancies are introduced into MoO<sub>3</sub> to form MoO<sub>3-x</sub>, LSPR occurs, and the light absorption range is broadened. Meanwhile, the oxygen vacancy can suppress the recombination of photogenerated carriers [97,104,105]. MoO<sub>3-x</sub> also often forms composite materials with other semiconductors to further improve the photocatalytic activity [98,101–103,125]. A Z-scheme CuS/MoO<sub>3-x</sub> heterostructured photocatalyst had been achieved successfully. With the abundant oxygen vacancies, MoO<sub>3-x</sub> exhibited a strong photosorption capacity in the visible region. The heterojunction interaction between CdS and MoO<sub>3-x</sub> promoted interfacial charge transfer, segregation, and migration of photoexcited charge carriers by decreasing the recombination of electron–hole pairs, and the CdS/MoO<sub>3-x</sub> showed an increasingly photocatalytic degradation performance of MO and TC with the increasing content of CuS within certain limits [98]. The morphology of ZnO nanomaterials can affect the LSPR, and research indicates that bowl-like and ring-like structures are beneficial for LSPR [106,107]. When oxides with oxygen vacancy defects are combined with other semiconductor materials to form composite photocatalysts, plasmonic hot electron injection and heterojunction structures usually exist according to the band structure to accelerate the separation of photocarriers, which is beneficial to improve the photocatalytic efficiency. The preparation, physical, and chemical properties and detailed photocatalytic performance of nonstoichiometric nonmetallic plasmonic photocatalysts are shown in Table 3.

The possible mechanism of self-doping nonstoichiometric nonmetallic plasmonic nanomaterials can usually be expressed as Figure 3. In self-doping nonstoichiometric nonmetallic plasmonic nanomaterials, oxygen vacancies form defect bands (DB) at the bottom of CB. The free electrons induced by the oxygen vacancy are excited to be hot electrons by SPR, and hot holes are left in the DB. Photoexcited electrons are captured in the DB and combine with hot holes to facilitate the separation of photogenerated carriers and accelerate the generation of hot electrons. Photogenerated electrons, holes, and hot electrons participate in the REDOX reaction.

**Table 3.** Summary of photocatalytic performances of nonstoichiometric nonmetallic plasmonic photocatalysts.

Materials	Preparation Method	Origin of LSPR	Structure	Light Source	Objects	Efficiency	Ref.
TiO <sub>2</sub> /W <sub>18</sub> O <sub>49</sub>	Two-step solvothermal procedure	W <sub>18</sub> O <sub>49</sub>	Sheet-like	Full spectrum	RhB	Degradation, 95.2% in 50 min	[75]
Cu <sub>2-x</sub> Se-g-C <sub>3</sub> N <sub>4</sub>	Solvent-thermal method	Cu <sub>2-x</sub> Se	—	Xe lamp	MB(2 × 10 <sup>-5</sup> M)	Degradation, 96.4% in 120 min	[88]
Cu <sub>1.8</sub> Se/Cu <sub>3</sub> Se <sub>2</sub>	Precipitation method	Cu <sub>2-x</sub> Se	A phase junction structure	Xe lamp(Vis and NIR)	MO(50 mg/L)	Degradation, 82% in 120 min	[91]
WO <sub>3-x</sub>	One-step template-free hydrothermal route	WO <sub>3-x</sub>	Staked morphology of nanosheets	Hg lamp (UV) visible light	RhB(2 × 10 <sup>-5</sup> M) RhB(2 × 10 <sup>-5</sup> M)	Degradation, 100% in 80 min Degradation, 77% in 320 min	[92]
W <sub>18</sub> O <sub>49</sub> /g-C <sub>3</sub> N <sub>4</sub>	Solvothermal method	W <sub>18</sub> O <sub>49</sub>	Nanorod bundles	Simulated sunlight	H <sub>2</sub>	Evolution, 15.2 μmol·h <sup>-1</sup>	[93]
CdS/WO <sub>3-x</sub>	Photoinduced electron injection	WO <sub>3-x</sub>	Bundles and nanowires	Visible-NIR light	H <sub>2</sub>	Evolution, 1.6 mmol·g <sup>-1</sup> ·h <sup>-1</sup>	[94]
MoO <sub>3-x</sub>	Solvothermal method	MoO <sub>3-x</sub>	Sheet-like	Xe lamp	MO (20 mg/L)	Degradation, 95.4% in 120 min	[97]
CdS/MoO <sub>3-x</sub>	One-pot hydrothermal method	MoO <sub>3-x</sub>	—	Visible light	MB (10 mgL <sup>-1</sup> ) TC (10 mg L <sup>-1</sup> )	Degradation, 97.6% Degradation, 85.5%	[98]
IO-TiO <sub>2</sub> -MoO <sub>3-x</sub>	Emulsion polymerization reaction + solvothermal method + calcination	MoO <sub>3-x</sub>	Honeycomb-like	Xe lamp	H <sub>2</sub> RhB	Evolution, 886 μmol/(g·h) Degradation, 90% in 60 min	[102]
MoO <sub>3-x</sub> /g-C <sub>3</sub> N <sub>4</sub>	Hydrothermally in situ growing	MoO <sub>3-x</sub>	—	Xe lamp	H <sub>2</sub>	Evolution 22.8 μmol/h	[103]
ZnO	Low-temperature chemical etching method	ZnO	Nanoplates Nanobowls Nanorings	UV	RhB	Degradation, 90% in 95 min Degradation, 90% in 83 min Degradation, 90% in 81 min	[106]
ZnO/rGO	One-step low-temperature chemical etching route	ZnO	Nanoplates Nanobowls Nanorings	Xe lamp	RhB (2 × 10 <sup>-5</sup> M)	Degradation, 90% in 140 min Degradation, 86% in 140 min Degradation, 97% in 140 min	[107]



### Self-doping nonstoichiometric nonmetallic plasmonic nanomaterials

**Figure 3.** The possible mechanism of self-doping nonstoichiometric nonmetallic plasmonic nanomaterials [97,98,128,131].

#### 4. Applications

As with the most common photocatalysts, photocatalysts consisting of these non-noble metals and nonmetallic plasmonic nanomaterials with LSPR effects are often used for both environmental remediation (photocatalytic removal of pollutants, photocatalytic sterilization) and energy conversion (photocatalytic H<sub>2</sub> production, photocatalytic CO<sub>2</sub> reduction, photocatalytic N<sub>2</sub> fixation, and photocatalytic alcohol conversion).

Along with the fast pace of the industrial age, a large number of pollutants have been released into the environment, causing serious environmental pollution. The photocatalytic removal of pollutants by means of plasmonic photocatalysts consisting of non-noble metals and nonmetallic nanomaterials is a promising technology. These plasmonic materials can make full use of their properties to efficiently remove pollutants using light as the driving force while reducing treatment costs and being non-toxic and non-hazardous to the environment. Zhang et al. [32] prepared Bi<sup>0</sup>/Bi<sub>2</sub>O<sub>3</sub>@C composites using a surfactant-assisted sol-gel method. Bi NPs were prepared by the in situ reduction of Bi<sub>2</sub>O<sub>3</sub> with amorphous carbon. The plasma Bi NPs produced hot carriers under visible light irradiation. Compared with bare Bi<sub>2</sub>O<sub>3</sub>, Bi<sup>0</sup>/Bi<sub>2</sub>O<sub>3</sub>@C showed a stronger degradation effect on methylene blue under sunlight. In 2017, Li et al. [75] prepared a hybrid photocatalyst with a broad-spectrum photocatalytic performance by in situ growing plasmonic W<sub>18</sub>O<sub>49</sub> nanocrystals on TiO<sub>2</sub> nanosheets, which can collect UV, visible, and NIR light to decompose organic pollutant RhB. Owing to the LSPR induced by an abundant oxygen vacancy in W<sub>18</sub>O<sub>49</sub>, the photocatalytic efficiency of TiO<sub>2</sub>/W<sub>18</sub>O<sub>49</sub> nanosheet samples is greatly improved compared with pure TiO<sub>2</sub> nanosheet samples. In Chen's study, a new high-efficiency Bi-modified Bi<sub>2</sub>S<sub>3</sub>-supported g-C<sub>3</sub>N<sub>4</sub>(BBC) plasmonic semiconductor photocatalyst has been successfully developed. The photocatalytic reduction of Cr(VI) and TC were used to investigate the photocatalytic performance of the samples. Due to the LSPR effect of Bi, the further development of charge separation and a good reaction interface, BBC shows the best photoreduction and photooxidation properties [40].

Plasmonic photocatalytic materials can absorb a wide spectrum of light (from UV to NIR) to photocatalytically kill bacteria, while the photothermal effect induced by LSPR can also inactivate bacteria, making plasmonic photocatalysis an efficient green and low-cost disinfection technology. Compared to high-cost noble metal plasmonic photocatalysts, nonnoble plasmonic materials and non-metallic plasmonic materials with photothermal synergistic catalysis have great potential in inactivating bacteria. In Maya Endo-Kimura's study, zero-valent Cu was deposited on the TiO<sub>2</sub> surface, and due to the LSPR effect of zero-valent Cu and the inherent nature of Cu, Cu/TiO<sub>2</sub> showed high bacterial inhibition against bacteria (*E. coli*) and fungi (*Aspergillus niger*) under visible light irradiation and dark conditions [132]. In 2022, a Zn<sub>2</sub>In<sub>2</sub>S<sub>5</sub>/W<sub>18</sub>O<sub>49</sub> composite was designed by Liu et al. Thanks to the synergistic effect of the z-scheme heterostructure and LSPR effect, the composite achieved 87.9% removal of TC after 60 min under vis-NIR illumination, while under the same conditions, it also achieved the complete inactivation of 8.3 log *E. coli*. Thus, they presented a credible photocatalytic reaction mechanism for antibiotic degradation and bacterial inactivation, which provides a new idea for the efficient photocatalytic treatment of practical wastewater [133].

Non-noble metal plasmonic materials and non-metallic plasmonic materials have a wide photo response range from UV to IR to maximize the use of sunlight and are also superior in addressing energy shortages through energy conversion, such as photocatalytic H<sub>2</sub> production and photocatalytic CO<sub>2</sub> reduction.

H<sub>2</sub> is an environmentally friendly alternative to fossil fuels, and photocatalytic hydrogen production is a promising pathway for hydrogen production. Huang et al. [50] prepared Cu/CG-1100 composite photocatalysts using chitosan graphene CG-1100 with folds, few layers, and special defects and Cu(Ac)<sub>2</sub> solution as raw materials using an in situ synthesis method under illumination. Using the LSPR effect of Cu NPs, the composite can reach a hydrogen production efficiency of 3.94 mmol·g<sup>-1</sup>·h<sup>-1</sup> and exhibit superior stability. In Zichao Lian's study, CdS/Cu<sub>9</sub>S<sub>5</sub> heterostructured nanocrystals were constructed,

exhibiting high and stable photocatalytic activity for an IR-induced hydrogen precipitation reaction with an apparent quantum yield of 4.4% at 1100 nm, and the tuning of the plasma p-n junction charge acceptor layer thickness was found to be an important factor in improving the catalytic activity [122].

Massive CO<sub>2</sub> emissions are causing global warming, and the solar-driven photoreduction of CO<sub>2</sub> to chemically added fuel is seen as a promising way to mitigate energy shortage and global warming. Tan et al. [52] used the hydrothermal method to deposit TiO<sub>2</sub> nanorod films on a transparent conductive substrate, followed by the electrochemical loading of Cu NPs to synthesize composites with photocatalytic activity to reduce CO<sub>2</sub> to CH<sub>4</sub> under UV irradiation. The plasmonic nature of Cu NPs greatly enhanced the photocatalytic activity of the material, and the CH<sub>4</sub> production rate could reach 2.91 ppm/gcatal·h, which was twice as high as that of the unmodified TiO<sub>2</sub> film. In Yue Huang's study, a one-dimensional/two-dimensional S-scheme W<sub>18</sub>O<sub>49</sub>/CdSe-diethylenetriamine photocatalyst with visible- to NIR-light-driven electron transport channels was constructed by the amination reaction of CdSe using a microwave solvothermal method, benefiting from the LSPR effect induced by oxygen vacancies in W<sub>18</sub>O<sub>49</sub> and the synergistic effect of coupling semiconductors to construct S-scheme heterojunctions, where highly efficient photocatalytic CO<sub>2</sub> reduction performance was achieved with a yield of 25.37 μmol h<sup>-1</sup>·g<sup>-1</sup>, which offers the possibility for the application of oxygen-vacancy-rich non-stoichiometric oxides for photocatalytic CO<sub>2</sub> reduction [126].

## 5. Conclusions

Plasmonic photocatalysts have attracted much attention for their abilities to exhibit a light absorption range from the UV region to NIF region and a high charge separation efficiency. In recent years, much research has been conducted to achieve plasmonic photocatalysts with a high photocatalytic performance and stability in terms of water splitting and organic pollutants degradation. Among plasmonic materials, plasmonic noble-metal-based photocatalytic materials are the most studied due to the wider light absorption range and the higher carrier separation efficiency. However, there are still some limitations of noble metal NPs for their development in practical application in the photocatalytic field due to their high cost, fixed plasma frequency, and low abundance. LSPRs have also been discovered in some non-noble metals and nonmetallic materials, including heavily doped semiconductors and metal oxides with a much lower density of free carriers than noble metals and longer wavelength for LSPR frequency and too lower photocatalytic activity to satisfy practical applications. Thus, achieving the higher photocatalytic activities of non-noble metal and nonmetallic plasmonic photocatalysts is very important. Currently, most studies on non-noble metal and nonmetallic plasmonic materials focus on broadening their optical response range, while the high free carrier separation efficiency and low photogenerated electron-hole pairs recombination efficiency are the keys to improve the photocatalytic activity of plasmonic photocatalysts. Therefore, enhancing the high free carrier separation efficiency and reducing photogenerated electron-hole pair's recombination efficiency could be hot spots in the further development of non-noble metal and nonmetallic plasmonic materials. For the construction of high-efficiency plasmonic photocatalysts, the following two points can be considered: (i) plasmonic material self-regulation, adjusting the plasmonic metal structure, morphology, and size to achieve spectral regulation and local field spatial enhancement, and controlling the composition and concentration of non-metallic plasmonic material host material and dopant to adjust the free carrier concentration to achieve the purpose of regulating the LSPR frequency. In addition, the exploration of suitable characterization methods is expected to achieve the design of plasmonic materials with an ideal carrier concentration. (ii) Combining with other materials to build composite photocatalysts: selecting materials with a suitable energy band structure for the composite, and modulating the spatial structure and energy band arrangement of the composite to increase the concentration of photogenerated carriers, regulate the light absorption range, inhibit photogenerated carrier compounding, increase the active site, improve the stability

of the material, and thus enhance the photocatalytic performance of the material, for example, increase the contact area between the plasmonic metal and the semiconductor so as to make full use of electromagnetic field enhancement to excite the semiconductor. This will offer new possibilities to achieve a higher photocatalytic activity for the removal of environmental pollutants and to solve energy shortage problems.

**Author Contributions:** Conceptualization, R.L.; investigation, X.W.; resources, R.L.; writing—original draft preparation, R.L.; writing—review and editing, X.W. and M.C.; funding acquisition, M.C. All authors have read and agreed to the published version of the manuscript.

**Funding:** This research was funded by [the 100 Talents initial Program of Chinese Academy of Sciences] grant number [E190620201].

**Data Availability Statement:** No new data were created or analyzed in this study. Data sharing is not applicable to this article.

**Conflicts of Interest:** The authors declare no conflict of interest.

## References

1. Li, C.; Yang, W.; Li, Q. TiO<sub>2</sub>-based photocatalysts prepared by oxidation of TiN nanoparticles and their photocatalytic activities under visible light illumination. *J. Mater. Sci. Technol.* **2018**, *34*, 969–975. [[CrossRef](#)]
2. Ben Saber, N.; Mezni, A.; Alrooqi, A.; Altalhi, T. Ternary Pt@TiO<sub>2</sub>/rGO Nanocomposite to Boost Photocatalytic Activity for Environmental and Energy Use. *J. Inorg. Organomet. Polym. Mater.* **2021**, *31*, 3802–3809. [[CrossRef](#)]
3. Lee, J.-H.; Ahn, H.-J.; Youn, J.-I.; Kim, Y.-J.; Suh, S.-J.; Oh, H.-J. Synthesis and Characterization of ZnO/TiO<sub>2</sub> Photocatalyst Decorated with PbS QDs for the Degradation of Aniline Blue Solution. *Korean J. Met. Mater.* **2018**, *56*, 900–909. [[CrossRef](#)]
4. Sheikhsamany, R.; Faghihian, H. Elimination of Phenylhydrazine from Aqueous Solutions by Use of a Photocatalyst Prepared by Immobilization of TiO<sub>2</sub> on Polypyrrole Support. *J. Inorg. Organomet. Polym. Mater.* **2019**, *30*, 1980–1989. [[CrossRef](#)]
5. Wang, Z.; Huang, B.; Wang, P.; Cheng, H.; Zheng, Z.; Lou, Z.; Dai, Y. Plasmonic Photocatalysts with Wide Light Absorption Spectra and High Charge Separation Efficiencies. In *From Molecules to Materials: Pathways to Artificial Photosynthesis*; Rozhkova, E.A., Ariga, K., Eds.; Springer International Publishing: Cham, Switzerland, 2015; pp. 241–267.
6. Li, Q.; Lei, S.; Li, Y.; Wang, Y.; Zhao, B.; Ruan, W. Investigation of compositionally tunable localized surface plasmon resonances (LSPRs) of a series of indium tin oxide nanocrystals prepared by one-step solvothermal synthesis. *J. Mater. Sci.* **2018**, *54*, 2918–2927. [[CrossRef](#)]
7. Chang, H.; Rho, W.-Y.; Son, B.S.; Kim, J.; Lee, S.H.; Jeong, D.H.; Jun, B.-H. Plasmonic Nanoparticles: Basics to Applications (I). In *Nanotechnology for Bioapplications*; Jun, B.H., Ed.; Springer: Berlin/Heidelberg, Germany, 2021; Volume 1309, pp. 133–159.
8. Zhang, S.; Li, J.; Wang, X.; Huang, Y.; Zeng, M.; Xu, J. In situ ion exchange synthesis of strongly coupled Ag@AgCl/g-C<sub>3</sub>N<sub>4</sub> porous nanosheets as plasmonic photocatalyst for highly efficient visible-light photocatalysis. *ACS Appl. Mater. Interfaces* **2014**, *6*, 22116–22125. [[CrossRef](#)]
9. Garcia-Peiro, J.I.; Bonet-Aleta, J.; Bueno-Alejo, C.J.; Hueso, J.L. Recent Advances in the Design and Photocatalytic Enhanced Performance of Gold Plasmonic Nanostructures Decorated with Non-Titania Based Semiconductor Hetero-Nanoarchitectures. *Catalysts* **2020**, *10*, 1459. [[CrossRef](#)]
10. Lu, W.; Qin, X.; Li, H.; Asiri, A.M.; Al-Youbi, A.O.; Sun, X.J.P.; Characterization, P.S. One-step hydrothermal synthesis of Ag nanoparticle decorated submicrometer-scale spherical AgBr colloids: A highly efficient visible light plasmonic photocatalyst for degradation of organic dyes. *Part. Part. Syst. Charact.* **2013**, *30*, 67–71. [[CrossRef](#)]
11. Xu, H.; Song, Y.; Liu, L.; Li, H.; Xu, Y.; Xia, J.; Wu, X.; Zhao, S. Plasmonic-enhanced visible-light-driven photocatalytic activity of Ag–AgBr synthesized in reactable ionic liquid. *J. Chem. Technol. Biotechnol.* **2012**, *87*, 1626–1633. [[CrossRef](#)]
12. Liang, Y.; Lin, S.; Liu, L.; Hu, J.; Cui, W. Facile hydrothermal synthesis of plasmonic photocatalyst Ag@AgCl and degradative photocatalysis under visible light irradiation. *J. Wuhan Univ. Technol. -Mater. Sci. Ed.* **2015**, *30*, 84–91. [[CrossRef](#)]
13. Jiang, L.; Zhou, G.; Mi, J.; Wu, Z. Fabrication of visible-light-driven one-dimensional anatase TiO<sub>2</sub>/Ag heterojunction plasmonic photocatalyst. *Catal. Commun.* **2012**, *24*, 48–51. [[CrossRef](#)]
14. Wei, W.; Jiang, Z.F.; Jing, J.J.; Lv, X.M.; Xie, J.M. Smart strategy to synthesis silver-based heterogeneous photocatalysts grown from molybdenum oxide precursor. *Micro Nano Lett.* **2017**, *12*, 978–981. [[CrossRef](#)]
15. Samanta, S.; Martha, S.; Parida, K. Facile Synthesis of Au/g-C<sub>3</sub>N<sub>4</sub> Nanocomposites: An Inorganic/Organic Hybrid Plasmonic Photocatalyst with Enhanced Hydrogen Gas Evolution Under Visible-Light Irradiation. *ChemCatChem* **2014**, *6*, 1453–1462.
16. Chang, A.; Peng, W.-S.; Tsai, I.T.; Chiang, L.-F.; Yang, C.-M. Efficient hydrogen production by selective alcohol photoreforming on plasmonic photocatalyst comprising sandwiched Au nanodisks and TiO<sub>2</sub>. *Appl. Catal. B: Environ.* **2019**, *255*, 117773. [[CrossRef](#)]
17. Cui, M.; Yu, J.; Lin, H.; Wu, Y.; Zhao, L.; He, Y. In-situ preparation of Z-scheme AgI/Bi<sub>5</sub>O<sub>7</sub>I hybrid and its excellent photocatalytic activity. *Appl. Surf. Sci.* **2016**, *387*, 912–920. [[CrossRef](#)]
18. Wen, X.-J.; Niu, C.-G.; Zhang, L.; Huang, D.-W.; Zeng, G.-M. In-situ synthesis of visible-light-driven plasmonic Ag/AgCl-CdWO<sub>4</sub> photocatalyst. *Ceram. Int.* **2017**, *43*, 1922–1929. [[CrossRef](#)]

19. Song, J.; Shi, Y.; Ren, M.; Hu, G. Synthesis, characterization and excellent photocatalytic activity of Ag/AgBr/MoO<sub>3</sub> composite photocatalyst. *Appl. Phys. A* **2014**, *116*, 2139–2147. [[CrossRef](#)]
20. Song, S.; Cheng, B.; Wu, N.; Meng, A.; Cao, S.; Yu, J. Structure effect of graphene on the photocatalytic performance of plasmonic Ag/Ag<sub>2</sub>CO<sub>3</sub>-rGO for photocatalytic elimination of pollutants. *Appl. Catal. B: Environ.* **2016**, *181*, 71–78. [[CrossRef](#)]
21. Ren, H.; Yang, J.-L.; Yang, W.-M.; Zhong, H.-L.; Lin, J.-S.; Radjenovic, P.M.; Sun, L.; Zhang, H.; Xu, J.; Tian, Z.-Q.; et al. Core-Shell-Satellite Plasmonic Photocatalyst for Broad-Spectrum Photocatalytic Water Splitting. *ACS Mater. Lett.* **2020**, *3*, 69–76. [[CrossRef](#)]
22. Wei, Z.; Benlin, D.; Fengxia, Z.; Xinyue, T.; Jiming, X.; Lili, Z.; Shiyin, L.; Leung, D.Y.C.; Sun, C. A novel 3D plasmonic p-n heterojunction photocatalyst: Ag nanoparticles on flower-like p-Ag<sub>2</sub>S/n-BiVO<sub>4</sub> and its excellent photocatalytic reduction and oxidation activities. *Appl. Catal. B: Environ.* **2018**, *229*, 171–180. [[CrossRef](#)]
23. Zhao, W.; Zhang, J.; Zhu, F.; Mu, F.; Zhang, L.; Dai, B.; Xu, J.; Zhu, A.; Sun, C.; Leung, D.Y.C. Study the photocatalytic mechanism of the novel Ag/p-Ag<sub>2</sub>O/n-BiVO<sub>4</sub> plasmonic photocatalyst for the simultaneous removal of BPA and chromium(VI). *Chem. Eng. J.* **2019**, *361*, 1352–1362. [[CrossRef](#)]
24. Shoueir, K.; Kandil, S.; El-hosainy, H.; El-Kemary, M. Tailoring the surface reactivity of plasmonic Au@TiO<sub>2</sub> photocatalyst bio-based chitosan fiber towards cleaner of harmful water pollutants under visible-light irradiation. *J. Clean. Prod.* **2019**, *230*, 383–393. [[CrossRef](#)]
25. Liang, X.; Wang, P.; Gao, Y.; Huang, H.; Tong, F.; Zhang, Q.; Wang, Z.; Liu, Y.; Zheng, Z.; Dai, Y.; et al. Design and synthesis of porous M-ZnO/CeO<sub>2</sub> microspheres as efficient plasmonic photocatalysts for nonpolar gaseous molecules oxidation: Insight into the role of oxygen vacancy defects and M=Ag, Au nanoparticles. *Appl. Catal. B: Environ.* **2020**, *260*, 118151. [[CrossRef](#)]
26. Endo-Kimura, M.; Kowalska, E. Plasmonic Photocatalysts for Microbiological Applications. *Catalysts* **2020**, *10*, 824. [[CrossRef](#)]
27. Khanam, S.; Rout, S.K. A Photocatalytic Hydrolysis and Degradation of Toxic Dyes by Using Plasmonic Metal-Semiconductor Heterostructures: A Review. *Chemistry* **2022**, *4*, 454–479. [[CrossRef](#)]
28. Ly, N.H.; Vasseghian, Y.; Joo, S.-W. Plasmonic photocatalysts for enhanced solar hydrogen production: A comprehensive review. *Fuel* **2023**, *344*, 128087. [[CrossRef](#)]
29. Li, Y.; Wang, S.; Zhao, Y.; Zhao, J.; Bouasavanh, S. SiO<sub>2</sub>-stabilized Bi nanoparticles: A high active and stable visible light photocatalyst. *Colloids Surf. A Physicochem. Eng. Asp.* **2019**, *567*, 112–120. [[CrossRef](#)]
30. Li, X.; Zhang, W.; Cui, W.; Sun, Y.; Jiang, G.; Zhang, Y.; Huang, H.; Dong, F. Bismuth spheres assembled on graphene oxide: Directional charge transfer enhances plasmonic photocatalysis and in situ DRIFTS studies. *Appl. Catal. B Environ.* **2018**, *221*, 482–489. [[CrossRef](#)]
31. Hao, Q.; Wang, R.; Lu, H.; Xie, C.a.; Ao, W.; Chen, D.; Ma, C.; Yao, W.; Zhu, Y. One-pot synthesis of C/Bi/Bi<sub>2</sub>O<sub>3</sub> composite with enhanced photocatalytic activity. *Appl. Catal. B Environ.* **2017**, *219*, 63–72. [[CrossRef](#)]
32. Zhang, L.; Ghimire, P.; Phuriragpitikhon, J.; Jiang, B.; Goncalves, A.A.S.; Jaroniec, M. Facile formation of metallic bismuth/bismuth oxide heterojunction on porous carbon with enhanced photocatalytic activity. *J. Colloid Interface Sci.* **2018**, *513*, 82–91. [[CrossRef](#)]
33. Huang, Y.; Kang, S.; Yang, Y.; Qin, H.; Ni, Z.; Yang, S.; Li, X. Facile synthesis of Bi/Bi<sub>2</sub>WO<sub>6</sub> nanocomposite with enhanced photocatalytic activity under visible light. *Appl. Catal. B Environ.* **2016**, *196*, 89–99. [[CrossRef](#)]
34. Wang, J.; Tang, L.; Zeng, G.; Liu, Y.; Zhou, Y.; Deng, Y.; Wang, J.; Peng, B. Plasmonic Bi Metal Deposition and g-C<sub>3</sub>N<sub>4</sub> Coating on Bi<sub>2</sub>WO<sub>6</sub> Microspheres for Efficient Visible-Light Photocatalysis. *ACS Sustain. Chem. Eng.* **2016**, *5*, 1062–1072. [[CrossRef](#)]
35. Liang, C.; Niu, C.G.; Zhang, L.; Wen, X.J.; Yang, S.F.; Guo, H.; Zeng, G.M. Construction of 2D heterojunction system with enhanced photocatalytic performance: Plasmonic Bi and reduced graphene oxide co-modified Bi<sub>5</sub>O<sub>7</sub>I with high-speed charge transfer channels. *J. Hazard. Mater.* **2019**, *361*, 245–258. [[CrossRef](#)]
36. Wang, H.; Yuan, X.; Wu, Y.; Zeng, G.; Tu, W.; Sheng, C.; Deng, Y.; Chen, F.; Chew, J.W. Plasmonic Bi nanoparticles and BiOCl sheets as cocatalyst deposited on perovskite-type ZnSn(OH)<sub>6</sub> microparticle with facet-oriented polyhedron for improved visible-light-driven photocatalysis. *Appl. Catal. B Environ.* **2017**, *209*, 543–553. [[CrossRef](#)]
37. Xie, Q.; He, W.; Liu, S.; Li, C.; Zhang, J.; Wong, P.K. Bifunctional S-scheme g-C<sub>3</sub>N<sub>4</sub>/Bi/BiVO<sub>4</sub> hybrid photocatalysts toward artificial carbon cycling. *Chin. J. Catal.* **2020**, *41*, 140–153. [[CrossRef](#)]
38. He, W.; Sun, Y.; Jiang, G.; Li, Y.; Zhang, X.; Zhang, Y.; Zhou, Y.; Dong, F. Defective Bi<sub>4</sub>MoO<sub>9</sub>/Bi metal core/shell heterostructure: Enhanced visible light photocatalysis and reaction mechanism. *Appl. Catal. B Environ.* **2018**, *239*, 619–627. [[CrossRef](#)]
39. Wang, H.; Zhang, W.; Li, X.; Li, J.; Cen, W.; Li, Q.; Dong, F. Highly enhanced visible light photocatalysis and in situ FT-IR studies on Bi metal@defective BiOCl hierarchical microspheres. *Appl. Catal. B Environ.* **2018**, *225*, 218–227. [[CrossRef](#)]
40. Chen, D.; Fang, J.; Lu, S.; Zhou, G.; Feng, W.; Yang, F.; Chen, Y.; Fang, Z. Fabrication of Bi modified Bi<sub>2</sub>S<sub>3</sub> pillared g-C<sub>3</sub>N<sub>4</sub> photocatalyst and its efficient photocatalytic reduction and oxidation performances. *Appl. Surf. Sci.* **2017**, *426*, 427–436. [[CrossRef](#)]
41. Sun, Y.; Zhao, Z.; Zhang, W.; Gao, C.; Zhang, Y.; Dong, F. Plasmonic Bi metal as cocatalyst and photocatalyst: The case of Bi/(BiO)<sub>2</sub>CO<sub>3</sub> and Bi particles. *J. Colloid Interface Sci.* **2017**, *485*, 1–10. [[CrossRef](#)]
42. Sun, D.; Huang, L.; Li, L.; Yu, Y.; Du, G.; Xu, B. Plasma enhanced Bi/Bi<sub>2</sub>O<sub>2</sub>CO<sub>3</sub> heterojunction photocatalyst via a novel in-situ method. *J. Colloid Interface Sci.* **2020**, *571*, 80–89. [[CrossRef](#)]
43. Shen, X.; Yang, Y.; Song, B.; Chen, F.; Xue, Q.; Shan, S.; Li, S. Magnetically recyclable and remarkably efficient visible-light-driven photocatalytic hexavalent chromium removal based on plasmonic biochar/bismuth/ferroferric oxide heterojunction. *J. Colloid Interface Sci.* **2021**, *590*, 424–435. [[CrossRef](#)] [[PubMed](#)]

44. Xu, X.; Meng, L.; Dai, Y.; Zhang, M.; Sun, C.; Yang, S.; He, H.; Wang, S.; Li, H. Bi spheres SPR-coupled Cu<sub>2</sub>O/Bi<sub>2</sub>MoO<sub>6</sub> with hollow spheres forming Z-scheme Cu<sub>2</sub>O/Bi/Bi<sub>2</sub>MoO<sub>6</sub> heterostructure for simultaneous photocatalytic decontamination of sulfadiazine and Ni(II). *J. Hazard Mater.* **2020**, *381*, 120953. [[CrossRef](#)] [[PubMed](#)]
45. Chen, Q.; Cheng, X.; Long, H.; Rao, Y. A short review on recent progress of Bi/semiconductor photocatalysts: The role of Bi metal. *Chin. Chem. Lett.* **2020**, *31*, 2583–2590. [[CrossRef](#)]
46. Gu, W.; Teng, F. SPR-promoted visible-light photocatalytic activity of Bi/ZIF hybrids. *J. Photochem. Photobiol. A Chem.* **2020**, *400*, 112679. [[CrossRef](#)]
47. Chava, R.K.; Son, N.; Kang, M. Bismuth quantum dots anchored one-dimensional CdS as plasmonic photocatalyst for pharmaceutical tetracycline hydrochloride pollutant degradation. *Chemosphere* **2022**, *300*, 134570. [[CrossRef](#)]
48. Ma, Z.-P.; Zhang, L.; Ma, X.; Shi, F.-N. Z-scheme g-C<sub>3</sub>N<sub>4</sub>/Bi/Bi<sub>3.64</sub>Mo<sub>0.36</sub>O<sub>6.55</sub> photocatalyst with dual charge transfer channels: Photodegradation of pollutants and mechanism insights. *Sep. Purif. Technol.* **2022**, *297*, 121435. [[CrossRef](#)]
49. Zhao, L.; Liu, Y.; Xi, X.; Shen, Y.; Wang, J.; Liu, Y.; Nie, Z. Bi/Bi<sub>2</sub>O<sub>3</sub>/WO<sub>3</sub> composite: A bifunctional plasmonic heterostructure for detection and degradation pollutions in wastewater. *J. Environ. Chem. Eng.* **2022**, *10*, 107643. [[CrossRef](#)]
50. Huang, T.; Xu, Z.; Zeng, G.; Zhang, P.; Song, T.; Wang, Y.; Wang, T.; Huang, S.; Wang, T.; Zeng, H. Selective deposition of plasmonic copper on few layers graphene with specific defects for efficiently synchronous photocatalytic hydrogen production. *Carbon* **2019**, *143*, 257–267. [[CrossRef](#)]
51. Zhang, P.; Zeng, G.; Song, T.; Huang, S.; Wang, T.; Zeng, H. Design of plasmonic CuCo bimetal as a nonsemiconductor photocatalyst for synchronized hydrogen evolution and storage. *Appl. Catal. B Environ.* **2019**, *242*, 389–396. [[CrossRef](#)]
52. Tan, J.Z.Y.; Fernández, Y.; Liu, D.; Maroto-Valer, M.; Bian, J.; Zhang, X. Photoreduction of CO<sub>2</sub> using copper-decorated TiO<sub>2</sub> nanorod films with localized surface plasmon behavior. *Chem. Phys. Lett.* **2012**, *531*, 149–154. [[CrossRef](#)]
53. Rekeb, L.; Hamadou, L.; Kadri, A.; Benbrahim, N.; Chainet, E. Highly broadband plasmonic Cu film modified Cu<sub>2</sub>O/TiO<sub>2</sub> nanotube arrays for efficient photocatalytic performance. *Int. J. Hydrogen Energy* **2019**, *44*, 10541–10553. [[CrossRef](#)]
54. Xiao, L.; Zhang, Q.; Chen, P.; Chen, L.; Ding, F.; Tang, J.; Li, Y.-J.; Au, C.-T.; Yin, S.-F. Copper-mediated metal-organic framework as efficient photocatalyst for the partial oxidation of aromatic alcohols under visible-light irradiation: Synergism of plasmonic effect and schottky junction. *Appl. Catal. B Environ.* **2019**, *248*, 380–387. [[CrossRef](#)]
55. Zhang, P.; Song, T.; Wang, T.; Zeng, H. Plasmonic Cu nanoparticle on reduced graphene oxide nanosheet support: An efficient photocatalyst for improvement of near-infrared photocatalytic H<sub>2</sub> evolution. *Appl. Catal. B Environ.* **2018**, *225*, 172–179. [[CrossRef](#)]
56. Gellé, A.; Moores, A. Water splitting catalyzed by titanium dioxide decorated with plasmonic nanoparticles. *Pure Appl. Chem.* **2017**, *89*, 1817–1827. [[CrossRef](#)]
57. Derikvandi, H.; Vosough, M.; Nezamzadeh-Ejhieh, A. A comprehensive study on the enhanced photocatalytic activity of a double-shell mesoporous plasmonic Cu(@)Cu<sub>2</sub>O/SiO<sub>2</sub> as a visible-light driven nanophotocatalyst. *Environ. Sci. Pollut. Res. Int.* **2020**, *27*, 27582–27597. [[CrossRef](#)] [[PubMed](#)]
58. Lai, H.; Xiao, W.; Wang, Y.; Song, T.; Long, B.; Yin, S.; Ali, A.; Deng, G.-J. Plasmon-induced carrier separation boosts high-selective photocatalytic CO<sub>2</sub> reduction on dagger-axe-like Cu@Co core-shell bimetal. *Chem. Eng. J.* **2021**, *417*, 129295. [[CrossRef](#)]
59. Xin, Y.; Yu, K.; Zhang, L.; Yang, Y.; Yuan, H.; Li, H.; Wang, L.; Zeng, J. Copper-Based Plasmonic Catalysis: Recent Advances and Future Perspectives. *Adv. Mater.* **2021**, *33*, e2008145. [[CrossRef](#)]
60. Yao, G.-Y.; Zhao, Z.-Y. Unraveling the role of cuprous oxide and boosting solar energy conversion via interface engineering in a Cu/TiO<sub>2</sub> plasmonic photocatalyst. *J. Mater. Chem. C* **2020**, *8*, 8567–8578. [[CrossRef](#)]
61. Zhang, P.; Liu, H.; Li, X. Plasmonic CuCo/Carbon Dots: An Unconventional Photocatalyst Used for Photocatalytic Overall Water Splitting. *ACS Sustain. Chem. Eng.* **2020**, *8*, 17979–17987. [[CrossRef](#)]
62. Zhang, P.; Liu, H.; Li, X. Plasmon-driven engineering in bimetallic CuCo combined with reduced graphene oxide for photocatalytic overall water splitting. *Appl. Surf. Sci.* **2021**, *559*, 149865. [[CrossRef](#)]
63. Zhang, P.; Liu, H.; Li, X. Photo-reduction synthesis of Cu nanoparticles as plasmon-driven non-semiconductor photocatalyst for overall water splitting. *Appl. Surf. Sci.* **2021**, *535*, 147720. [[CrossRef](#)]
64. Zhou, L.; Martinez, J.M.P.; Finzel, J.; Zhang, C.; Swearer, D.F.; Tian, S.; Robotjazi, H.; Lou, M.; Dong, L.; Henderson, L.; et al. Light-driven methane dry reforming with single atomic site antenna-reactor plasmonic photocatalysts. *Nat. Energy* **2020**, *5*, 61–70. [[CrossRef](#)]
65. Dai, B.; Zhao, W.; Huang, H.; Li, S.; Yang, G.; Wu, H.; Sun, C.; Leung, D.Y.C. Constructing an ohmic junction of copper@ cuprous oxide nanocomposite with plasmonic enhancement for photocatalysis. *J. Colloid Interface Sci.* **2022**, *616*, 163–176. [[CrossRef](#)] [[PubMed](#)]
66. Hao, Q.; Wang, C.; Huang, H.; Li, W.; Du, D.; Han, D.; Qiu, T.; Chu, P.K. Aluminum plasmonic photocatalysis. *Sci. Rep.* **2015**, *5*, 15288. [[CrossRef](#)]
67. Robotjazi, H.; Lou, M.; Clark, B.D.; Jacobson, C.R.; Swearer, D.F.; Nordlander, P.; Halas, N.J. Site-Selective Nanoreactor Deposition on Photocatalytic Al Nanocubes. *Nano Lett.* **2020**, *20*, 4550–4557. [[CrossRef](#)]
68. Wang, C.; Yang, W.-C.D.; Raciti, D.; Bruma, A.; Marx, R.; Agrawal, A.; Sharma, R. Endothermic reaction at room temperature enabled by deep-ultraviolet plasmons. *Nat. Mater.* **2020**, *20*, 346–352. [[CrossRef](#)]
69. Yuan, L.; Lou, M.; Clark, B.D.; Lou, M.; Zhou, L.; Tian, S.; Jacobson, C.R.; Nordlander, P.; Halas, N.J. Morphology-Dependent Reactivity of a Plasmonic Photocatalyst. *ACS Nano* **2020**, *14*, 12054–12063. [[CrossRef](#)]

70. Zhang, C.; Zhao, H.; Zhou, L.; Schlather, A.E.; Dong, L.; McClain, M.J.; Swearer, D.F.; Nordlander, P.; Halas, N.J. Al-Pd Nanodisk Heterodimers as Antenna-Reactor Photocatalysts. *Nano Lett.* **2016**, *16*, 6677–6682. [[CrossRef](#)]
71. Zhou, L.; Zhang, C.; McClain, M.J.; Manjavacas, A.; Krauter, C.M.; Tian, S.; Berg, F.; Everitt, H.O.; Carter, E.A.; Nordlander, P.; et al. Aluminum Nanocrystals as a Plasmonic Photocatalyst for Hydrogen Dissociation. *Nano Lett.* **2016**, *16*, 1478–1484. [[CrossRef](#)]
72. Jiang, Q.; Ji, C.; Riley, D.J.; Xie, F. Boosting the efficiency of photoelectrolysis by the addition of non-noble plasmonic metals: Al & Cu. *Nanomaterials* **2018**, *9*, 1.
73. Liu, J.; Xu, M.; Zhang, T.; Chu, X.; Shi, K.; Li, J. Al/TiO<sub>2</sub> composite as a photocatalyst for the degradation of organic pollutants. *Environ. Sci. Pollut. Res. Int.* **2023**, *30*, 9738–9748. [[CrossRef](#)]
74. Mangrulkar, P.A.; Chilkalwar, A.A.; Kotkondawar, A.V.; Manwar, N.R.; Antony, P.S.; Hippargi, G.; Labhsetwar, N.; Trachtenberg, M.C.; Rayalu, S.S. Plasmonic nanostructured Zn/ZnO composite enhances carbonic anhydrase driven photocatalytic hydrogen generation. *J. CO<sub>2</sub> Util.* **2017**, *17*, 207–212. [[CrossRef](#)]
75. Li, J.; Li, W.; Li, X.; Li, Y.; Bai, H.; Li, M.; Xi, G. Plasmonic W<sub>18</sub>O<sub>49</sub>-photosensitized TiO<sub>2</sub> nanosheets with wide-range solar light harvesting. *RSC Adv.* **2017**, *7*, 23846–23850. [[CrossRef](#)]
76. Zhuang, T.-T.; Liu, Y.; Li, Y.; Zhao, Y.; Wu, L.; Jiang, J.; Yu, S.-H. Integration of Semiconducting Sulfides for Full-Spectrum Solar Energy Absorption and Efficient Charge Separation. *Angew. Chem.-Int. Ed.* **2016**, *55*, 6396–6400. [[CrossRef](#)] [[PubMed](#)]
77. Franzen, S. Surface plasmon polaritons and screened plasma absorption in indium tin oxide compared to silver and gold. *J. Phys. Chem. C* **2008**, *112*, 6027–6032. [[CrossRef](#)]
78. Huang, H.; Hao, Q.; Fan, X.; Luo, Z.; Hou, X.; Yang, X.; Qiu, T.; Chu, P.K. Self-assembled bundled TiO<sub>2</sub> nanowire arrays encapsulated with indium tin oxide for broadband absorption in plasmonic photocatalysis. *Phys. Chem. Chem. Phys.* **2017**, *19*, 27059–27064. [[CrossRef](#)]
79. Huang, H.; Fan, X.; Hao, Q.; Du, D.; Luo, X.; Qiu, T. Exploring indium tin oxide capped titanium dioxide nanolace arrays for plasmonic photocatalysis. *RSC Adv.* **2016**, *6*, 12611–12615. [[CrossRef](#)]
80. Riley, C.T.; Smalley, J.S.; Post, K.W.; Basov, D.N.; Fainman, Y.; Wang, D.; Liu, Z.; Sirbuly, D.J. High-Quality, Ultraconformal Aluminum-Doped Zinc Oxide Nanoplasmonic and Hyperbolic Metamaterials. *Small* **2016**, *12*, 892–901. [[CrossRef](#)] [[PubMed](#)]
81. Guillén, C.; Herrero, J. Structural and plasmonic characteristics of sputtered SnO<sub>2</sub>:Sb and ZnO:Al thin films as a function of their thickness. *J. Mater. Sci.* **2016**, *51*, 7276–7285. [[CrossRef](#)]
82. Paria, D.; Vadakkumbatt, V.; Ravindra, P.; Avasthi, S.; Ghosh, A. Unconventional plasmonic sensitization of graphene in mid-infrared. *Nanotechnology* **2021**, *32*, 315202. [[CrossRef](#)]
83. Ye, X.; Reifsnnyder Hickey, D.; Fei, J.; Diroll, B.T.; Paik, T.; Chen, J.; Murray, C.B. Seeded growth of metal-doped plasmonic oxide heterodimer nanocrystals and their chemical transformation. *J. Am. Chem. Soc.* **2014**, *136*, 5106–5115. [[CrossRef](#)]
84. Gordon, T.R.; Paik, T.; Klein, D.R.; Naik, G.V.; Caglayan, H.; Boltasseva, A.; Murray, C.B. Shape-dependent plasmonic response and directed self-assembly in a new semiconductor building block, indium-doped cadmium oxide (ICO). *Nano Lett.* **2013**, *13*, 2857–2863. [[CrossRef](#)]
85. Wolf, A.; Hartling, T.; Hinrichs, D.; Dorfs, D. Synthesis of plasmonic Cu<sub>2-x</sub>Se@ZnS core@shell nanoparticles. *Chemphyschem* **2016**, *17*, 717–723. [[CrossRef](#)] [[PubMed](#)]
86. Poulouse, A.C.; Veeranarayanan, S.; Mohamed, M.S.; Aburto, R.R.; Mitcham, T.; Bouchard, R.R.; Ajayan, P.M.; Sakamoto, Y.; Maekawa, T.; Kumar, D.S. Multifunctional Cu<sub>2-x</sub>Te Nanocubes Mediated Combination Therapy for Multi-Drug Resistant MDA MB 453. *Sci. Rep.* **2016**, *6*, 35961. [[CrossRef](#)]
87. Cui, J.; Li, Y.; Liu, L.; Chen, L.; Xu, J.; Ma, J.; Fang, G.; Zhu, E.; Wu, H.; Zhao, L.; et al. Near-Infrared Plasmonic-Enhanced Solar Energy Harvest for Highly Efficient Photocatalytic Reactions. *Nano Lett.* **2015**, *15*, 6295–6301. [[CrossRef](#)] [[PubMed](#)]
88. Han, J.; Zou, H.Y.; Liu, Z.X.; Yang, T.; Gao, M.X.; Huang, C.Z. Efficient visible-light photocatalytic heterojunctions formed by coupling plasmonic Cu<sub>2-x</sub>Se and graphitic carbon nitride. *New J. Chem.* **2015**, *39*, 6186–6192. [[CrossRef](#)]
89. Marbella, L.E.; Gan, X.Y.; Kaseman, D.C.; Millstone, J.E. Correlating Carrier Density and Emergent Plasmonic Features in Cu<sub>2-x</sub>Se Nanoparticles. *Nano Lett.* **2017**, *17*, 2414–2419. [[CrossRef](#)] [[PubMed](#)]
90. Kwon, Y.-T.; Lim, G.-D.; Kim, S.; Ryu, S.H.; Hwang, T.-Y.; Park, K.-R.; Choa, Y.-H. Near-infrared absorbance properties of Cu<sub>2-x</sub>S/SiO<sub>2</sub> nanoparticles and their PDMS-based composites. *J. Mater. Chem. C* **2018**, *6*, 754–760. [[CrossRef](#)]
91. Qiao, L.-N.; Wang, H.-C.; Shen, Y.; Lin, Y.-H.; Nan, C.-W. Enhanced Photocatalytic Performance under Visible and Near-Infrared Irradiation of Cu<sub>1.8</sub>Se/Cu<sub>3</sub>Se<sub>2</sub> Composite via a Phase Junction. *Nanomaterials* **2017**, *7*, 19. [[CrossRef](#)]
92. Chen, S.; Xiao, Y.; Xie, W.; Wang, Y.; Hu, Z.; Zhang, W.; Zhao, H. Facile strategy for synthesizing non-stoichiometric monoclinic structured tungsten trioxide (WO<sub>3-x</sub>) with plasma resonance absorption and enhanced photocatalytic activity. *Nanomaterials* **2018**, *8*, 553. [[CrossRef](#)]
93. Zhang, Z.; Huang, J.; Fang, Y.; Zhang, M.; Liu, K.; Dong, B. A Nonmetal Plasmonic Z-Scheme Photocatalyst with UV- to NIR-Driven Photocatalytic Protons Reduction. *Adv. Mater.* **2017**, *29*, 1606688. [[CrossRef](#)] [[PubMed](#)]
94. Lou, Z.; Zhu, M.; Yang, X.; Zhang, Y.; Whangbo, M.-H.; Li, B.; Huang, B. Continual injection of photoinduced electrons stabilizing surface plasmon resonance of non-elemental-metal plasmonic photocatalyst CdS/WO<sub>3-x</sub> for efficient hydrogen generation. *Appl. Catal. B Environ.* **2018**, *226*, 10–15. [[CrossRef](#)]
95. Lu, C.; Li, J.; Chen, G.; Li, B.; Lou, Z. Self-Z-scheme plasmonic tungsten oxide nanowires for boosting ethanol dehydrogenation under UV-visible light irradiation. *Nanoscale* **2019**, *11*, 12774–12780. [[CrossRef](#)] [[PubMed](#)]

96. Lu, C.; Li, J.; Yan, J.; Li, B.; Huang, B.; Lou, Z. Surface plasmon resonance and defects on tungsten oxides synergistically boost high-selective CO<sub>2</sub> reduction for ethylene. *Appl. Mater. Today* **2020**, *20*, 100744. [CrossRef]
97. Liu, Q.; Wu, Y.; Zhang, J.; Chen, K.; Huang, C.; Chen, H.; Qiu, X. Plasmonic MoO<sub>3-x</sub> nanosheets with tunable oxygen vacancies as efficient visible light responsive photocatalyst. *Appl. Surf. Sci.* **2019**, *490*, 395–402. [CrossRef]
98. Wu, Y.; Wang, H.; Tu, W.; Wu, S.; Chew, J.W. Construction of hole-transported MoO<sub>3-x</sub> coupled with CdS nanospheres for boosting photocatalytic performance via oxygen-defects-mediated Z-scheme charge transfer. *Appl. Organomet. Chem.* **2019**, *33*, e4780. [CrossRef]
99. Etman, A.S.; Abdelhamid, H.N.; Yuan, Y.; Wang, L.; Zou, X.; Sun, J. Facile Water-Based Strategy for Synthesizing MoO<sub>3-x</sub> Nanosheets: Efficient Visible Light Photocatalysts for Dye Degradation. *ACS Omega* **2018**, *3*, 2193–2201. [CrossRef]
100. Jin, L.; Zheng, X.; Liu, W.; Cao, L.; Cao, Y.; Yao, T.; Wei, S. Integration of plasmonic and amorphous effects in MoO<sub>3-x</sub> spheres for efficient photoelectrochemical water oxidation. *J. Mater. Chem. A* **2017**, *5*, 12022–12026. [CrossRef]
101. Wen, M.; Song, S.; Liu, Q.; Yin, H.; Mori, K.; Kuwahara, Y.; Li, G.; An, T.; Yamashit, H. Manipulation of plasmon-induced hot electron transport in Pd/MoO<sub>3-x</sub>@ZIF-8: Boosting the activity of Pd-catalyzed nitroaromatic hydrogenation under visible-light irradiation. *Appl. Catal. B Environ.* **2021**, *282*, 119511. [CrossRef]
102. Lv, C.; Wang, L.; Liu, X.; Zhao, L.; Lan, X.; Shi, J. An efficient inverse opal (IO)-TiO<sub>2</sub>-MoO<sub>3-x</sub> for photocatalytic H<sub>2</sub> evolution and RhB degradation—The synergy effect of IO structure and plasmonic MoO<sub>3-x</sub>. *Appl. Surf. Sci.* **2020**, *527*, 146726. [CrossRef]
103. Guo, Y.; Chang, B.; Wen, T.; Zhang, S.; Zeng, M.; Hu, N.; Su, Y.; Yang, Z.; Yang, B. A Z-scheme photocatalyst for enhanced photocatalytic H<sub>2</sub> evolution, constructed by growth of 2D plasmonic MoO<sub>3-x</sub> nanoplates onto 2D g-C<sub>3</sub>N<sub>4</sub> nanosheets. *J. Colloid Interface Sci.* **2020**, *567*, 213–223. [CrossRef] [PubMed]
104. Bai, H.; Yi, W.; Li, J.; Xi, G.; Li, Y.; Yang, H.; Liu, J. Direct growth of defect-rich MoO<sub>3-x</sub> ultrathin nanobelts for efficiently catalyzed conversion of isopropyl alcohol to propylene under visible light. *J. Mater. Chem. A* **2016**, *4*, 1566–1571. [CrossRef]
105. Li, J.; Ye, Y.; Ye, L.; Su, F.; Ma, Z.; Huang, J.; Xie, H.; Doronkin, D.E.; Zimina, A.; Grunwaldt, J.-D.; et al. Sunlight induced photo-thermal synergistic catalytic CO<sub>2</sub> conversion via localized surface plasmon resonance of MoO<sub>3-x</sub>. *J. Mater. Chem. A* **2019**, *7*, 2821–2830. [CrossRef]
106. Zhao, Y.; Cui, T.; Wu, T.; Jin, C.; Qiao, R.; Qian, Y.; Tong, G. Polymorphous ZnO nanostructures: Zn polar surface-guided size and shape evolution mechanism and enhanced photocatalytic activity. *ChemCatChem* **2017**, *9*, 3180–3190. [CrossRef]
107. Zhao, Y.; Liu, L.; Cui, T.; Tong, G.; Wu, W. Enhanced photocatalytic properties of ZnO/reduced graphene oxide sheets (rGO) composites with controllable morphology and composition. *Appl. Surf. Sci.* **2017**, *412*, 58–68. [CrossRef]
108. Blemker, M.A.; Gibbs, S.L.; Raulerson, E.K.; Milliron, D.J.; Roberts, S.T. Modulation of the Visible Absorption and Reflection Profiles of ITO Nanocrystal Thin Films by Plasmon Excitation. *ACS Photonics* **2020**, *7*, 1188–1196. [CrossRef]
109. Hosseinpour, Z.; Hosseinpour, S. Facile synthesis of Er:CuS flowers and their application in the photo-catalytic activity. *Mater. Sci. Semicond. Process.* **2017**, *72*, 32–36. [CrossRef]
110. Ma, L.; Chen, S.; Shao, Y.; Chen, Y.-L.; Liu, M.-X.; Li, H.-X.; Mao, Y.-L.; Ding, S.-J. Recent progress in constructing plasmonic metal/semiconductor hetero-nanostructures for improved photocatalysis. *Catalysts* **2018**, *8*, 634. [CrossRef]
111. Ma, X.C.; Dai, Y.; Yu, L.; Huang, B.B. Energy transfer in plasmonic photocatalytic composites. *Light Sci. Appl.* **2016**, *5*, e16017. [CrossRef]
112. Hao, Y.-J.; Li, F.-T.; Wang, S.-S.; Chai, M.-J.; Liu, R.-H.; Wang, X.-J. One-step combustion synthesis of β-Bi<sub>2</sub>O<sub>3</sub>-NiO/Ni composites and their visible light photocatalytic performance. *Mater. Sci. Eng. B* **2014**, *186*, 41–47. [CrossRef]
113. Pan, L.; Zhu, Y.; Wang, Z.; Xu, X.; He, H.; Du, W.; Hu, J.; Zhou, Y. Plasmonic Cocatalyst with Electric and Thermal Stimuli Boosts Solar Hydrogen Evolution. *Sol. RRL* **2020**, *4*, 2000094. [CrossRef]
114. Talebi, P.; Kistanov, A.A.; Rani, E.; Singh, H.; Pankratov, V.; Pankratova, V.; King, G.; Huttula, M.; Cao, W. Unveiling the role of carbonate in nickel-based plasmonic core@shell hybrid nanostructure for photocatalytic water splitting. *Appl. Energy* **2022**, *322*, 119461. [CrossRef]
115. Ullah, I.; Ling, C.; Li, J.-H.; Lu, X.-J.; Li, C.; Yang, Z.; Qian, X.-J.; Wang, G.; Xu, A.-W. Metallic plasmons significantly boosted visible-light photocatalytic hydrogen evolution from water splitting. *Sustain. Energy Fuels* **2023**, *7*, 263–269. [CrossRef]
116. Matsko, N.L. Formation of normal surface plasmon modes in small sodium nanoparticles. *Phys. Chem. Chem. Phys.* **2020**, *22*, 13285–13291. [CrossRef]
117. Gutiérrez, Y.; Giangregorio, M.M.; Palumbo, F.; González, F.; Brown, A.S.; Moreno, F.; Losurdo, M. Sustainable and Tunable Mg/MgO Plasmon-Catalytic Platform for the Grand Challenge of SF<sub>6</sub> Environmental Remediation. *Nano Lett.* **2020**, *20*, 3352–3360. [CrossRef]
118. Hopper, E.R.; Boukouvala, C.; Asselin, J.; Biggins, J.S.; Ringe, E. Opportunities and Challenges for Alternative Nanoplasmonic Metals: Magnesium and Beyond. *J. Phys. Chem. C* **2022**, *126*, 10630–10643. [CrossRef] [PubMed]
119. Hopper, E.R.; Wayman, T.M.R.; Asselin, J.; Pinho, B.; Boukouvala, C.; Torrente-Murciano, L.; Ringe, E. Size Control in the Colloidal Synthesis of Plasmonic Magnesium Nanoparticles. *J. Phys. Chem. C* **2022**, *126*, 563–577. [CrossRef]
120. Gordillo, N.; Catalán-Gómez, S.; Pau, J.L.; Redondo-Cubero, A. Spectrally broad plasmonic absorption in Ga and In nanoparticle hybrids. *Nanotechnology* **2019**, *30*, 475705. [CrossRef]
121. Chen, C.-Y.; Chien, C.-Y.; Wang, C.-M.; Lin, R.-S.; Chen, I.C. Plasmon Tuning of Liquid Gallium Nanoparticles through Surface Anodization. *Materials* **2022**, *15*, 2145. [CrossRef]

122. Lian, Z.; Wu, F.; Zhong, Y.; Zi, J.; Li, Z.; Wang, X.; Nakagawa, T.; Li, H.; Sakamoto, M. Tuning plasmonic p–n junction for efficient infrared-light-responsive hydrogen evolution. *Appl. Catal. B Environ.* **2022**, *318*, 121860. [[CrossRef](#)]
123. Li, N.; Fan, H.; Zhao, W.; Gao, Y.; Ge, L. 2D/0D plasmonic CuSe/CdS for efficient photocatalytic hydrogen activity via strong Vis-NIR light and interfacial effect. *Appl. Surf. Sci.* **2022**, *590*, 153028. [[CrossRef](#)]
124. Liu, X.; Yang, L.; Huang, M.; Li, Q.; Zhao, L.; Sang, Y.; Zhang, X.; Zhao, Z.; Liu, H.; Zhou, W. Oxygen vacancy-regulated metallic semiconductor MoO<sub>2</sub> nanobelt photoelectron and hot electron self-coupling for photocatalytic CO<sub>2</sub> reduction in pure water. *Appl. Catal. B Environ.* **2022**, *319*, 121887. [[CrossRef](#)]
125. Ren, Y.; Feng, D.; Yan, Z.; Sun, Z.; Zhang, Z.; Xu, D.; Qiao, C.; Chen, Z.; Jia, Y.; Chan Jun, S.; et al. Interfacial coupled engineering of plasmonic amorphous MoO<sub>3–x</sub> nanodots/g-C<sub>3</sub>N<sub>4</sub> nanosheets for photocatalytic water splitting and photothermal conversion. *Chem. Eng. J.* **2023**, *453*, 139875. [[CrossRef](#)]
126. Huang, Y.; Dai, K.; Zhang, J.; Dawson, G. Photocatalytic CO<sub>2</sub> conversion of W<sub>18</sub>O<sub>49</sub>/CdSe-Diethylenetriamine with high charge transfer efficiency: Synergistic effect of LSPR effect and S-scheme heterojunction. *Chin. J. Catal.* **2022**, *43*, 2539–2547. [[CrossRef](#)]
127. Ji, S.; Dong, J.; Ji, M.; Zou, W.; Yin, S.; Chen, Z.; Xia, J. Rapid dual-channel electrons transfer via synergistic effect of LSPR effect and build-in electric field in Z-scheme W<sub>18</sub>O<sub>49</sub>/BiOBr heterojunction for organic pollutants degradation. *Inorg. Chem. Commun.* **2022**, *138*, 109283. [[CrossRef](#)]
128. Lu, Y.; Jia, X.; Ma, Z.; Li, Y.; Yue, S.; Liu, X.; Zhang, J. W<sup>5+</sup>–W<sup>5+</sup> Pair Induced LSPR of W<sub>18</sub>O<sub>49</sub> to Sensitize ZnIn<sub>2</sub>S<sub>4</sub> for Full-Spectrum Solar-Light-Driven Photocatalytic Hydrogen Evolution. *Adv. Funct. Mater.* **2022**, *32*, 2203638. [[CrossRef](#)]
129. He, X.; Liu, Q.; Xu, D.; Wang, L.; Tang, H. Plasmonic TiN nanobelts assisted broad spectrum photocatalytic H<sub>2</sub> generation. *J. Mater. Sci. Technol.* **2022**, *116*, 1–10. [[CrossRef](#)]
130. Zhang, M.; Tang, L.; Duan, A.; Zhang, Y.; Xiao, F.; Zhu, Y.; Wang, J.; Feng, C.; Yin, N. Adjusting charge kinetics of conjugated polymers via integration of LSPR effect with homojunction. *Chem. Eng. J.* **2023**, *452*, 139068. [[CrossRef](#)]
131. Tan, X.; Wang, L.; Cheng, C.; Yan, X.; Shen, B.; Zhang, J. Plasmonic MoO<sub>3–x</sub>@MoO<sub>3</sub> nanosheets for highly sensitive SERS detection through nanoshell-isolated electromagnetic enhancement. *Chem. Commun.* **2016**, *52*, 2893–2896. [[CrossRef](#)]
132. Endo-Kimura, M.; Karabiyik, B.; Wang, K.; Wei, Z.; Ohtani, B.; Markowska-Szczupak, A.; Kowalska, E. Vis-Responsive Copper-Modified Titania for Decomposition of Organic Compounds and Microorganisms. *Catalysts* **2020**, *10*, 1194. [[CrossRef](#)]
133. Liu, H.-Y.; Niu, C.-G.; Guo, H.; Huang, D.-W.; Liang, C.; Yang, Y.-Y.; Tang, N.; Zhang, X.-G. Integrating the Z-scheme heterojunction and hot electrons injection into a plasmonic-based Zn<sub>2</sub>In<sub>2</sub>S<sub>5</sub>/W<sub>18</sub>O<sub>49</sub> composite induced improved molecular oxygen activation for photocatalytic degradation and antibacterial performance. *J. Colloid Interface Sci.* **2022**, *610*, 953–969. [[CrossRef](#)] [[PubMed](#)]

**Disclaimer/Publisher’s Note:** The statements, opinions and data contained in all publications are solely those of the individual author(s) and contributor(s) and not of MDPI and/or the editor(s). MDPI and/or the editor(s) disclaim responsibility for any injury to people or property resulting from any ideas, methods, instructions or products referred to in the content.